

5.3. Phantom Radiation Profiles

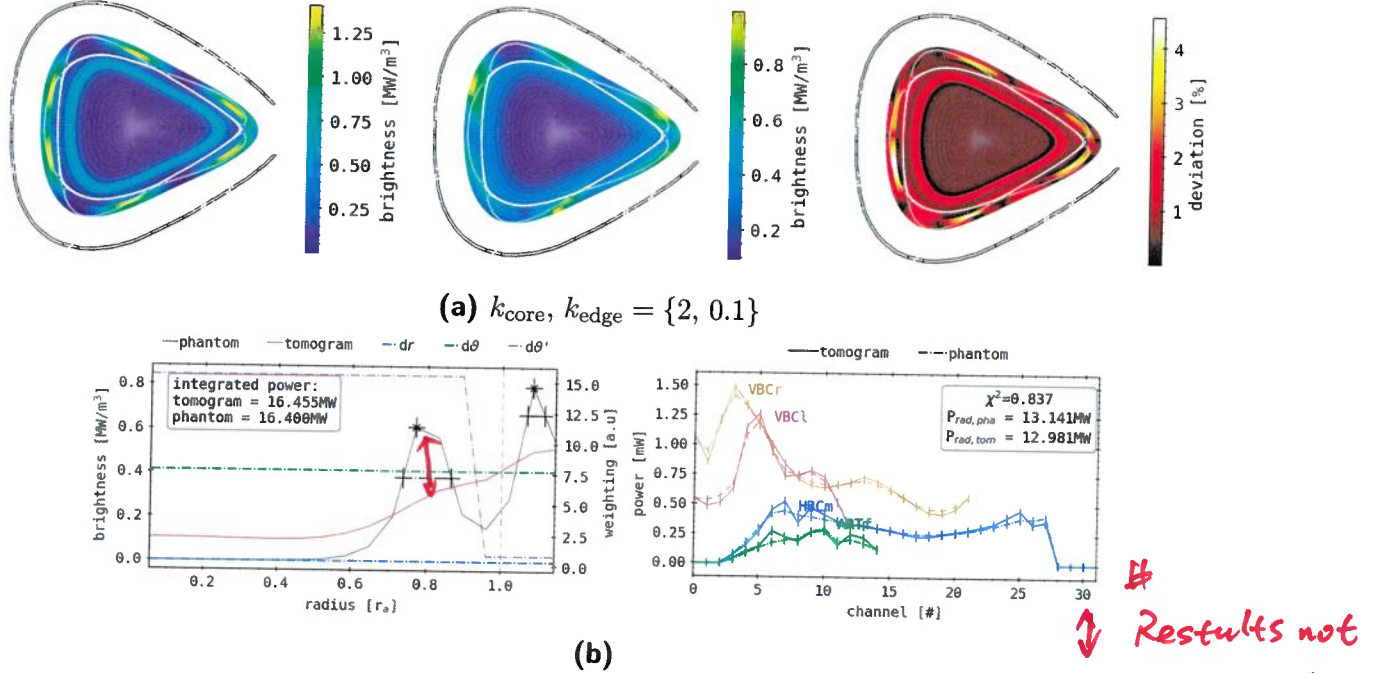


Figure 5.32.: Phantom radiation distribution reconstruction, mimicking a bright core and islands-like structures in the edge like in figure 5.30. In this case, the camera system is extended by an artificial, secondary horizontal camera on the opposite (poloidally) side of the HBCm - its geometry has been introduced in figure 5.15. The chosen RDA coefficients support the reconstruction of the given phantom distribution. **(a)** Phantom, tomogram and relative deviance, similar to figure 5.18. **(b)** Radial (left) and chordal (right) profile analysis, similar to figure 5.19. The new camera *MIRh* has been added in the chord brightness profile.

latter structures feature a slightly increased radial width compared to the phantom, while some also partially extend beyond the LCFS and towards the domain boundary, i.e.inboard and at the bottom middle X-point. They are accompanied by an also radially smoothed and symmetrical core ring of 0.5 MW/m^3 , coincidentally lacking the visible separation from the SOL emissivity into which it blends over.

On the right, the MSD yields a maximum error of 4.6 % outside the separatrix, precisely where the input phantoms bright spots are located, except

for the top outboard and inboard pseudo magnetic islands. In-between in smaller groupings, towards the LCFS and slightly beyond into the core, deviation values of 1.6–2 % are presented. A minor gap in radial direction is followed by a concentrated ring around $0.7r_a$ with a discrepancy of 2.2 % and a smooth core at $<1\%$.

In figure 5.32:(b), the usual composition of radial, anisotropic and forward calculated detector signal profiles are shown, accompanied by the singular two- and one-dimensional integrated power values. The shown regularisation weight and k_{ani} , as well as the phantoms poloidally averaged plots are the same as before. Though the general shape of the tomograms profile is similar, the minor peaks found previously for reconstructions of this artificial emissivity distribution are negligible here. In $0.8r_a$ and $1.1r_a$, small variations in the increasing slope in brightness from $0.5r_a$ and 0.1 – 0.52 MW/m^3 at the boundary are shown. Inside the core, up until the latters base point, the brightness is relatively constant around 0.95 MW/m^3 . An integrated power of $P_{\text{rad},2D} = 16.455 \text{ MW/m}^3$ corresponds to a 0.3 % deviation from the phantom. On the right, the individual camera forward calculated signals are extended by the results for ARTf. Qualitatively, the reconstructed results are similar to those from before, i.e. in figure 5.30:(b), though the per-absorber

deviation is minutely increased, partially beyond the given confidence intervals for the vertical cameras. With respect to the extremum features presented in the phantoms profiles of all cameras, the tomograms lines are less articulated here compared to the previous results. The new artificial array yields signals of up to a maximum of 0.3 mW for both images, while the phantom shows a steady and smooth increase from channel no. two through ten after which a minor drop to 0.15 mW in no. eleven and conclusively 0.1 mW in no. 14 follows. Around detector no six and twelve, the phantoms plot presents noticeably pronounced local maxima beyond the error bars up to 0.3 mW . Extrapolation using the absorber data from the artificial profile finds $P_{\text{rad}} = 13.141 \text{ MW}$ and the reconstructed image 12.981 MW , yielding a 1.2 % deviation and an overall fitness of the tomogram of $\chi^2 = 0.837 \text{ a. u.}$

With respect to the first set of results in figure 5.30 and constant k_{ani} , the MFR employing an additional set of LOS from the artificial MIRh presents a subjectively improved radiation profile with significantly more distinct and accurately localised spots in the SOL. No improvement can be noticed in the separation or intensity of the emissivity inside the separatrix. However, judging from the poloidally averaged and forward calculated, one-

*Shorten
the text!*

dimensional plots, including the integrated powers and fitness coefficient, a quantitative upgrade can hardly be argued for, especially given the previously examined variability in those parameters for different regularisation weights. This furthermore does not equate to a degradation in MFR results, though it can be concluded that the complementary detectors and their area of observations yield a positive effect on the tomographies quality for complex, superimposed radiation profiles of this kind. Conceptually, assuming that the point-of-view and orientation of the new camera significantly differs from the others, adding more LOS and therefore measurement points undeniably enhances the regularisation capabilities. Most critically, at least $(N_{HBC} + N_{VBC_r})$ and at most $N \times (N_{HBC} + N_{VBC_r})$ new intersections contribute to the algorithmic inversion and the N new absorber to $\mathbf{T} \in \mathbb{R}^{n \times m}$ - remember that n is the total number of absorbers and \mathbf{T} the transmission matrix. As discussed earlier, this also makes the geometric expression of local sensitivity more robust towards perturbations, as one can trivially verify using the same argument regarding the norm of the extended \mathbf{T}' and its condition $\kappa(\mathbf{T}')$, see Ghaoui et al.[193].

Inverted Anisotropic Phantom

For sake of completion, an inverted phantom to the original in figure 5.30 and 5.31 is reconstructed using an also reversed regularisation weight profile with $k_{ani} = \{0.3, 0.2\}$, and shape given by section 5.1.1. The ~~artificial radiation distribution~~ and MFR results are shown in figure 5.33 in the usual form.

On the left, the inside-out turned phantom shows a maximum brightness of 1.2 MW/m^3 , now in the core at $0.7r_a$ in eight up-down symmetrically distributed localised spots. Analytically, this profile can also be described by equation (5.20) when parametrically reconfigured with $r_{0,1} = 1.1r_a$ and $r_{0,2} = 0.7r_a$, i.e. the reversed order from before. Hence, a smooth ring of 1 MW/m^3 is found outside the separatrix in the SOL. Challenging with this particular phantom tomography is the potential obfuscation due to possibly increased interference from the symmetrical structure, given the position and orientation of the vertical and horizontal bolometer cameras. In the center of (a), the tomogram shows a continuous emissivity at the domain boundary and towards $1.1r_a$ of 0.55 MW/m^3 . This is followed by a comparatively sharp drop inwards to 0.35 MW/m^3 beyond the separatrix until $0.7r_a$ with

Phantom
 (≠ tomogram
 in figure 5.30,
 and 5.31)

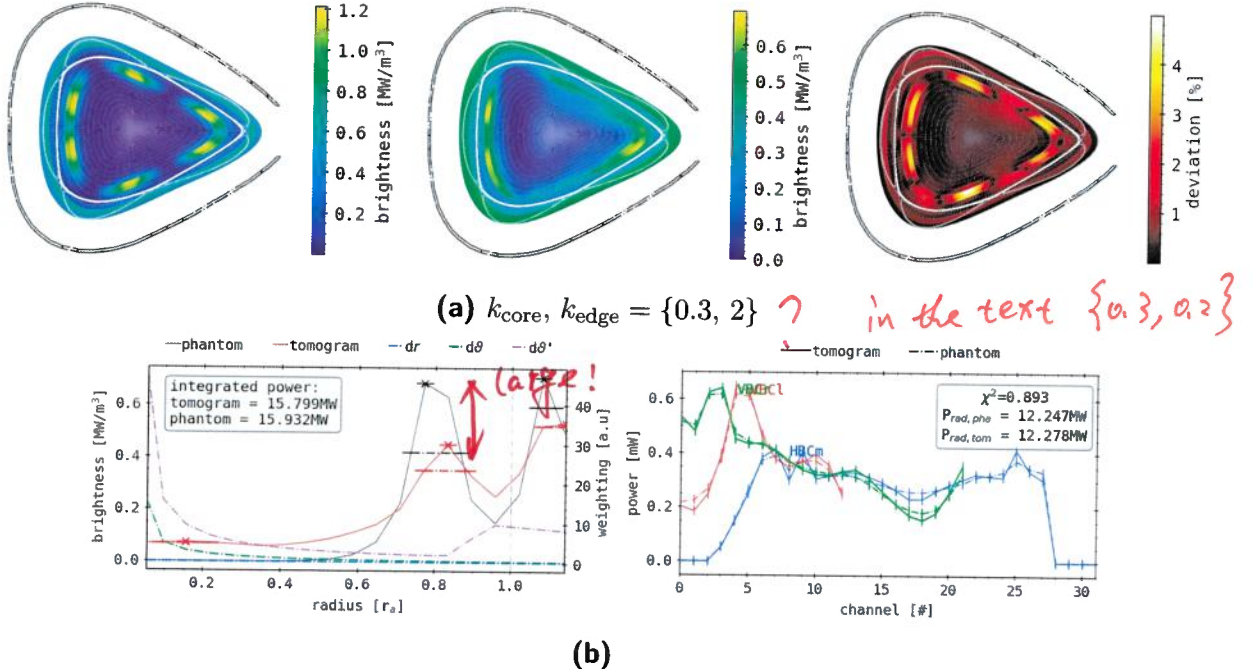


Figure 5.33.: Phantom radiation distribution reconstruction, mimicking a bright outside ring and islands-like structures on the inside of that ring, similar to figure 5.30 but inverted. The RDA coefficients have been changed accordingly to accompany the different orientation of poloidally symmetric and anisotropic radiation distributions. (a, top) Phantom, tomogram and relative deviance, similar to figure 5.18. (b) Radial (left) and chordal (right) profile analysis, similar to figure 5.19.

minor, unstructured variability in-between. At that radius, three prominent features can be found around the triangular plane: two, nearly symmetrical elongated bright spots towards the inboard magnetic island, separated by a small local minimum, where the lower is slightly increased in size and one larger at the outboard tip, extending into the lower half. All the prior have a strongly localised maxima of 0.69 MW/m^3 . Secondary, significantly weaker characteristics present close to the central top and bottom X-points at that same radius with $<0.5 \text{ MW/m}^3$, isolated by distinct voids in brightness. For $< 0.7r_a$, only minor emissivities of $<0.45 \text{ MW/m}^3$ are shown towards to the upper magnetic islands.

5.3. Phantom Radiation Profiles

On the right in figure 5.33:(a), the MSD almost exclusively consists of and is dominated by six individual, sharply pronounced areas in locations of the original input characteristics with maximum error values of 4.9 %. Otherwise, no significant deviation besides small variations in-between those localisations >1.6 % can be found.

Below on the left in (b), a combined poloidally averaged profile of phantom and tomogram are shown. The prior increases quickly from $0.5r_a$ outward until $0.75r_p$ to 0.7 MW/m^3 in a peak of $0.15r_a$ FWHM. After a distinct valley of 0.15 MW/m^3 in $0.95r_a$, a second and conclusive, sharper peak to 0.675 MW/m^3 with a width of $0.05r_a$ follows, which decays to 0.5 MW/m^3 at the boundary. The phantoms plot is constant at 0.6 MW/m^3 in the core until $0.4r_a$ and increases from there parabolically in its first peak of $0.1r_a$ width to 0.45 MW/m^3 in $0.83r_a$. A higher, in the same location as before positioned local minimum of 0.25 MW/m^3 is concluded by again a second maximum at the edge of the domain with 0.57 MW/m^3 . Using equation (5.16), the two-dimensional phantom and tomogram radiation image yield 15.932 MW and 15.799 MW respectively, corresponding to 0.08 % deviation.

Shorten

the

text!

On the right in figure 5.33:(b), forward calculated camera profiles of the artificial emissivity distribution show significantly smaller maxima when compared to the original phantom in figure 5.30. The VBCl shows 0.605 mW in channel no. four, coinciding with the inboard side magnetic island, tangent to the separatrix, decaying quickly towards no. zero at the edge and inward to no. eight. A small bump to 0.395 mW and plateau with a conclusive drop provides the transition to the right side array results of the core. Decreasing from 0.35 mW in absorber no. 21 to 0.198 mW in no. 18, the VBCr profile increases gradually from there with small variations until the detectors viewing the outboard side separatrix and SOL, i.e. no. five through one, between which also 0.605 mW is measured by channel no. two and three. The horizontal camera produces a relatively flat plot between 0.27–0.4 mW, where the shallow minimum is found in the core by absorber no. 18. Just inside the two-sided sharp increase from no. two and 28, the arrays maximum measurements of 0.4 mW and 0.36 mW are indicated by detectors no. seven and 25 respectively, aligning with the upper and lower part of the SOL and LCFS. Small, local extremes with $\leq 0.1 \text{ mW}$ relative amplitude are presented around the prior global maxima. The forward integrated absorber signals from the tomograms' emissivity distribution are generally within the provided individual confidence intervals, while being

slightly more pronounced in locations of the aforementioned extremes. In a few cases, i.e. the VBCl channel no. one, VBCr and HBCm no. 17 and 18 or no. 25, the particular characteristics are amplified by <0.05 mW beyond that range. Extrapolation of the provided profiles yields $P_{\text{rad}} = 12.247$ MW from the phantom and 12.278 MW from the tomogram, a 1.09 % deviation that correlates well with the noted fitness factor of $\chi^2 = 0.893$ a. u..

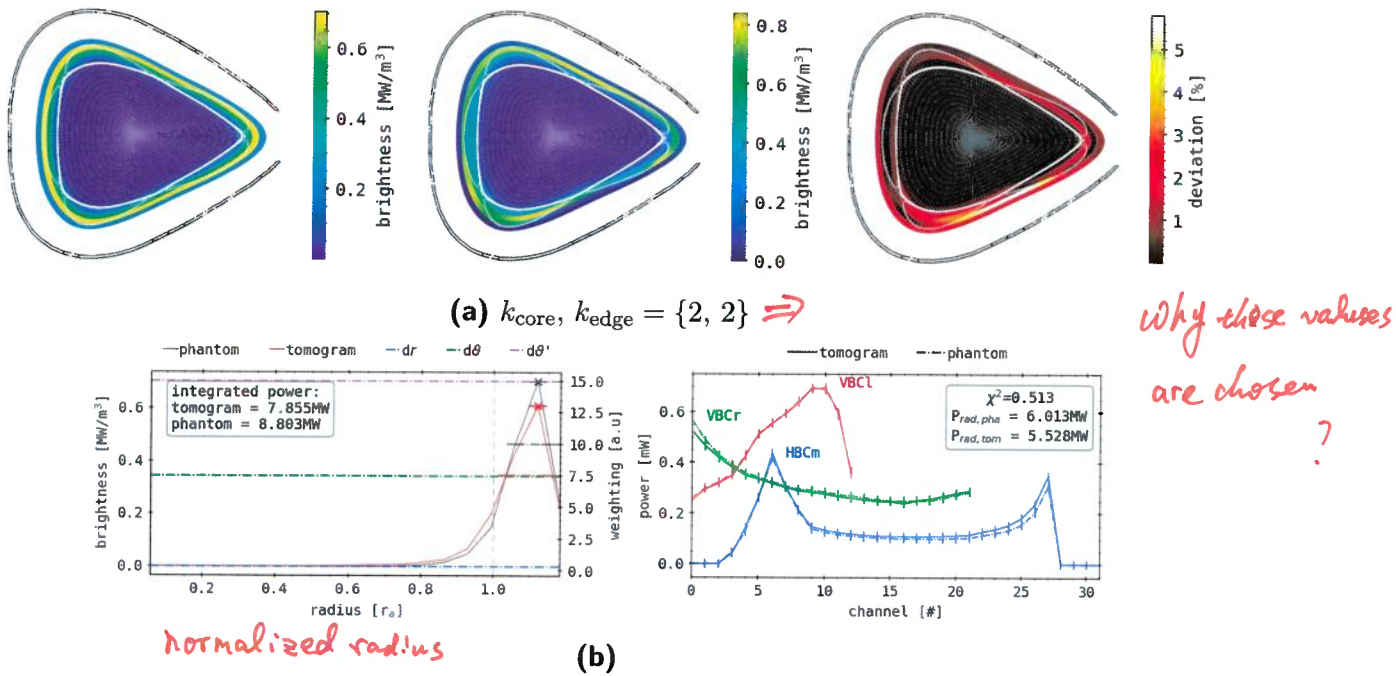
In terms of - subjectively measured - reconstruction quality, this type of artificial emissivity superposition shows greater discrepancies for the same approach and settings when compared to the prior, inverted case in figure 5.31 and following. Due to the switched radial orientation of the employed contrasting profiles, the increased sensitivity of the bolometer camera detectors in the SOL and along the separatrix leads to an *obfuscating* effect on the anisotropic core structure. More specifically, the focus of the tomogram is entirely changed, certainly also due to the reversed k_{ani} regularisation weighting, placing the majority of the brightness in that area, expanding until the edge of the domain. The maximum emissivity is found in the core still, in locations similar to those in the phantom, though with greatly decreased resolution and accuracy. Features vertically above the VBC arrays are entirely missing, coinciding with the LOS with the most unfavourable ratio between integration lengths through SOL and anisotropic core profiles. However, this is contrasted by the noticeably and significantly improved match between the poloidally averaged and forward integrated results, their corresponding power values $P_{\text{rad},2D}$ and P_{rad} , as well as the better fitness χ^2 . In summary, similar experimentally measured radiation distributions will potentially be even more difficult to reconstruct adequately in terms of quality of more focused or localised features, respective their shape and relative intensity.

5.3.4. Geometry Error Propagation for Reconstructions

A conclusive, necessary step before statistically exploring the MFR method in more detail and applying the gained experience in tandem with the tomography of experimental bolometer data is to gauge the impact of faulty assumptions or measurement errors in the camera geometry and by extension the transmission matrix T . The goal here is the find out if and how big of an influence the propagation of alignment errors or discrepancies in the determination of the pinhole (i.e. camera) position has on the final quality of the tomogram. Premise for this approach is the *directed* deviation of all

The best pair
of Kore, Kedge
should be used
for this study.
But

5.3. Phantom Radiation Profiles



LOS, i.e. all pinholes and absorbers are shifted in the same way with respect to their assumed geometry, so that the perturbed LOS fan yields a distinct and significant rotation compared to its original orientation. Furthermore, this particular effect is to be unknown and only affects the calculation of the pseudo-measurements as input for the MFR, which is performed still with the benchmark geometry. For this very purpose, a fairly simple, symmetrical and most importantly already examined and reconstructed phantom radiation profile will be used, and a reconstruction performed using the also previously introduced LOS geometries with $\pm 1^\circ$ poloidal tilt from the *as-designed* con-

struction. Details respective their setup can be found in section 5.2.2. The baseline artificial brightness distribution and MFR as a benchmark will be that of figure 5.18 and section 5.3.1, a symmetrical, thin ring of radiation in $r_0 = 1.1r_a$ with no anisotropic variation, using a uniform $k_{\text{ani}} = \{2, 2\}$. In both cases, the entirety of the multicamera bolometer system has been rotated collectively by the given angle around their corresponding aperture center locations in clockwise (*positive*) or counter-clockwise (*negative*) direction.

The first set of results can be found in figure 5.34 and features the original phantom and reconstructed tomogram based off of the *as-designed* LOS system, as well as the forward integrated signals from the phantom, achieved with the misaligned geometry and used for the reconstruction and their reverse counterpart as before. At the center of (a), the tomogram places stronger asymmetries at and around the bottom inboard, on the edge of the lower outboard and in-between the upper two magnetic islands. Their individual maximum brightness is higher than the intensity of the input ring at $>0.7 \text{ MW/m}^3$, with 0.85 MW/m^3 the global peak in the latter location. Along $1.1r_a$, the emissivity is at least 0.6 MW/m^3 , except for a large gap towards the lower outboard field structure where it drops to 0.35 MW/m^3 . Coincidentally, the MSD profile yields the largest error values in that area with a large, expanded feature of 5.7 % between the two neighbouring islands. The remaining deviations are far below at $\leq 2.5 \%$ around the triangular plane, while minor variations can be found towards the edge where the emissivity in the tomogram was broadened.

In (b) on the left, both poloidally averaged profiles find the global maximum at $1.12r_a$, while the tomograms result is slightly lowered from 0.7 MW/m^3 to 0.6 MW/m^3 . Both peaks have a very similar rise and decay, and the same FWHM of $0.15r_a$. However, despite the strong agreement in the radial profile, integration of the two-dimensional distributions in phantom and tomogram provide $P_{\text{rad},2D} = 8.803 \text{ MW}$ and 7.855 MW respectively, which equals a 12 % difference. Obviously, the parameterised regularisation weight profile is flat at $k_{\text{ani}} = k_{\text{core}} = k_{\text{core}} = 15 \text{ a.u.}$

On the right, the forward integrated signals of phantom and tomogram are shown. Like described above, results from the artificial distribution are produced using the geometry with the $+1^\circ$ tilt in clockwise direction, while the back-calculated profiles from the tomogram are achieved by integration with the *as-designed* LOS alignment. Overall shape and characteristics of

the plots are the same as in the initial MFR of this particular image, i.e. in figure 5.19. As in the latter, the horizontal cameras detectors indicate a noticeable asymmetry in both profiles, though the structure is the same towards and around each portion of the array that tangentially views a part of the separatrix. With respect to the established benchmark of this artificial distribution, the discrepancy between detectors viewing the upper and lower portion of the SOL is markedly reduced here from being half to just 0.06 mW difference in peak value. In the phantom, absorbers with LOS through the lower half of the triangular plane find lower emissivity values compared to the already reduced results from the tomogram. Although the integral power per channel is still within the corresponding error confidence interval, a relatively consistent deviation of $\sim 7.5\%$ can be found from no. ten onwards. The VBCr shows the reverse behaviour, where absorbers towards the outboard side, watching the SOL and LCFS yield higher brightness measurements of the same rate from channel no. five through zero. On the other side, the left vertical bolometer camera presents no significant variance between the two plots, besides a negligible decrease in the reconstructed results closer to the core, i.e. detectors no. three and below. In contrast to the visually well-matching profiles, extrapolation of the shown absorber signals indicates a large discrepancy with $P_{\text{rad}} = 6.013 \text{ MW}$ and 5.528 MW , a 5.9% error between phantom and tomogram respectively. Comparing this to the first MFR of this artificial distribution, this is a 5.7% deviation. The low fitness factor of $\chi^2 = 0.513 \text{ a. u.}$ underlines the latter observation.

A second set of results for the corresponding rotation of the LOS fans of all three cameras by -1° is shown in figure 5.35 and presented in the same way for also the same set of k_{ani} . In the center of (a), the phantom features an asymmetry and global maximum of 0.87 MW/m^3 around the inside edge of the upper inboard magnetic islands that extends along the $1.1r_a$ radius also towards the inboard side. A minor, secondary maximum of 0.7 MW/m^3 is located similarly to before between the lower two field structures in the SOL, while the rest of the ring is greatly reduced in brightness down to 0.45 MW/m^3 . Radially, its width is slightly increased to $\sim 0.2r_a$ compared to the phantom around the extremes and narrower elsewhere. Correspondingly, the MSD on the right shows large error values where the global maximum was found of up to 4.6% and smaller ones of 3.2% in the lower outboard magnetic island. The remaining SOL yields deviations $\leq 2.4\%$.

The tomograms poloidally averaged profile in figure 5.35:(b) is noticeably

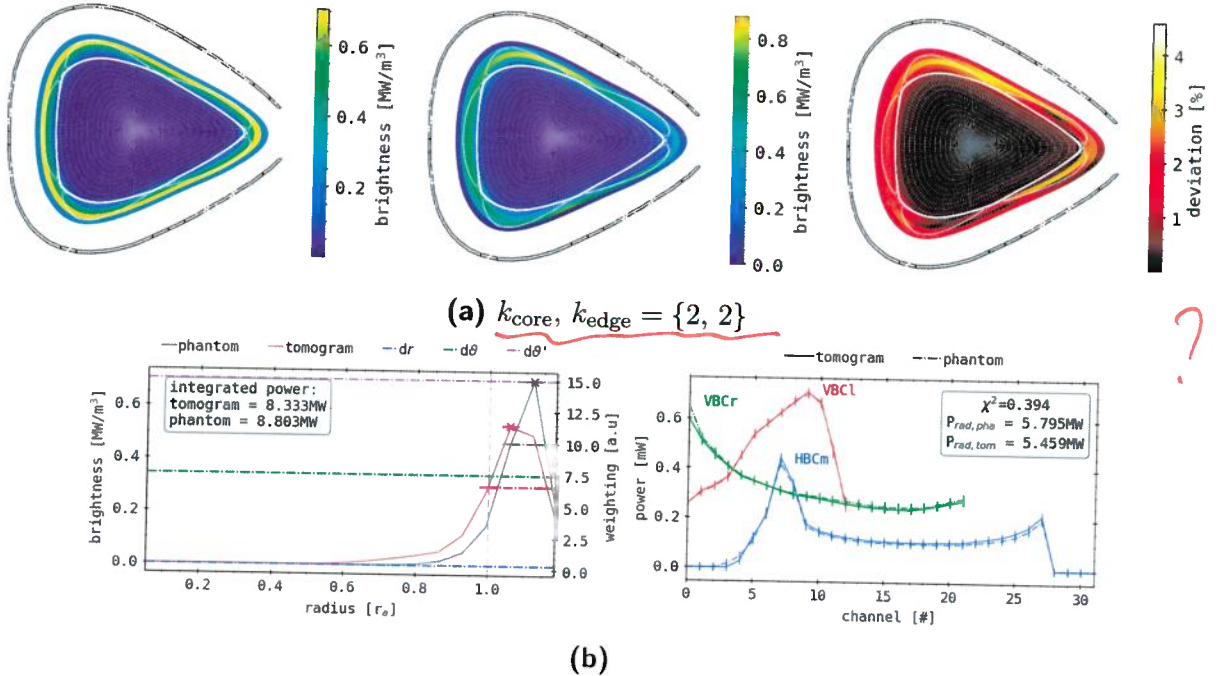


Figure 5.35.: Same phantom radiation distribution and reconstruction problem as in figure 5.35, but for a camera geometry rotation of -1° .
(a) Phantom, tomogram and relative deviance, similar to figure 5.18. **(b)** Radial (left) and chordal (right) profile analysis, similar to figure 5.19.

shifted towards the separatrix and core. All the profile inside and outside the LCFS is moved by $0.06r_a$ closer to the magnetic axis, including the location of the minutely reduced peak of 0.5 MW/m^3 in $1.05r_a$, though its width is increased to $0.16r_a$. In this case, the integrated power is higher at $P_{\text{rad},2D} = 8.333 \text{ MW}$, which is 6.1 % larger than its previous counterpart and decreased by 6.3 % respective the phantom baseline.

The previously examined and discussed dissymmetry in the HBCm results is amplified here on the lower side viewing the SOL, i.e. channel no. three through twelve, where the forward integrated signals are now double that of the opposite side, no. 23 through 27 in both phantom and tomogram. Otherwise, core and overall profile are qualitatively similar compared to figure 5.34. The prior shows about 0.1 mW like before, same as the aforementioned asymmetry on the left of up to 0.44 mW , hence a reduction to

0.21 mW from the absorbers viewing the upper SOL. No significant changes with respect to the initial benchmark can be found for the vertical bolometer array detectors. Like the last set of forward calculations, deviations between tomogram and phantom plot for all cameras are limited to the provided error confidence interval, though in contrast not particularly elevated in or around extremes. Extrapolation of the erroneous artificial radiation image results yields a slightly reduced $P_{\text{rad}} = 5.795$ MW compared to before and of the corresponding tomogram 5.4595 MW, equalling a 4.6% and 6.2% decrease, which also is a 1.8% raise with respect to the first set of numbers in figure 5.19. Finally, again clashing with the observations above is a weak fitness of $\chi^2 = 0.394$ a. u..

The criticality and importance concerning the underlying issue of this examination towards the MFR and its performance is highlighted by the variance of P_{rad} across the different sets of results. In this case, substantial increments compared to the baseline geometry extrapolation are found from the faulty profiles. Furthermore, the reproduced two-dimensional emissivity distributions show noticeable and particular characteristics that align with the designed error in the LOS orientation. Similarly, particularly in the HBCm forward calculated measurements, a correlating effect of the rotation on the shape and intrinsic asymmetry of the profile is very prominent. A significantly worse fitness coefficient compared to the previous supports the above findings, though the detector signal integration trend towards the *actual* radiation powers yield the contrary picture. From the presented impact of a distinct error in the transmission matrix T , unfortunately no other attribute than the increased or decreased characteristic in the individual camera results for symmetrical radiation distributions definitively points towards such underlying discrepancies. In a worst case scenario like this cumulative deviation in the location measurement of the bolometer or changes in its construction alignment, a divergence of $\geq 10\%$ in both singular absorber data and tomogram values are to be expected and in an experimental context nearly impossible to account for.

5.3.5. Reconstructive Limits

The conclusive, final next step before approaching actual experimental data with the MFR algorithm and RDA method is the quantitative, i.e. statistical evaluation of the above explored, simple phantom emissivity distributions.

Do you define them as two or our method?
Maybe "RDA-based MFR"?

This section will focus on systematic iteration of the anisotropic regularisation weights k_{core} and k_{edge} individually over across larger spectra than before and recording the findings of the reconstruction for simple artificial images, i.e. a *bright ring* like before in section 5.3.1. For this purpose, the previously introduced and examined characteristics, i.e. extremes location and FWHM, *mean squared deviation* (MSD) of equation (5.14), integrated two-dimensional power values from the phantom and tomogram and the fitness factor χ^2 . At this opportunity, an additional measure is introduced to gauge the agreement between input and output of the algorithm. The *Pearson¹ correlation coefficient (PCC)* ρ_c or $\rho_{x,y}$ between quantities x and y measures their linear correlation. The number ρ_c is the ratio of covariances and product of their respective standard deviations, therefore its result is binned by $[-1, 1]$. Let $E(\vec{x})$ be the *expected value* of variable \vec{x} , i.e. the vectorized representation of the phantom or tomogram like in equation (5.6) and section 5.3.3. The Pearson coefficient hence can be written as:

$$E(\vec{x}) = \frac{1}{n_r n_\theta} \sum_{i=0}^{n_r n_\theta} x^{(i)} \stackrel{!}{=} \bar{x},$$

$$\rho_{x,y} = \rho_C(\vec{x}, \vec{y}) = \frac{E((\vec{x} - E(\vec{x}) \cdot \vec{1})(\vec{y} - E(\vec{y}) \cdot \vec{1}))}{\sqrt{\vec{x} - E(\vec{x}) \cdot \vec{1}} \sqrt{\vec{y} - E(\vec{y}) \cdot \vec{1}}} ,$$

$$\stackrel{!}{=} \frac{1}{\sigma_{\vec{x}} \sigma_{\vec{y}}} \text{cov}(\vec{x}, \vec{y}). \quad (5.21)$$

Isotropic Ring Combinations

In figure 5.36, these particular sets of attributes are collected for a simple artificial radiation distribution consisting of a singular bright ring at $0.5r_a$ after the example in figure 5.18. The left and right plot series are split into the individual k_{core} and k_{edge} variations across ranges of $[0.65, 1]$ a.u. and $[1.25, 1.8]$ a.u. respectively. While one of those is altered, the other is kept at unity, i.e. $k_{\text{ani}} = 1$ a.u., yielding no change in regularisation. From top to bottom, the presented images show: the global maximum brightness radial location, its full width at half maximum height (FWHM), individual core, SOL and total MSD according to equation (5.14), the core and absolute

¹Karl Pearson, FRS, FRSE * Mar 27, 1857 †Apr. 17, 1936; English mathematician and biostatistician

5.3. Phantom Radiation Profiles

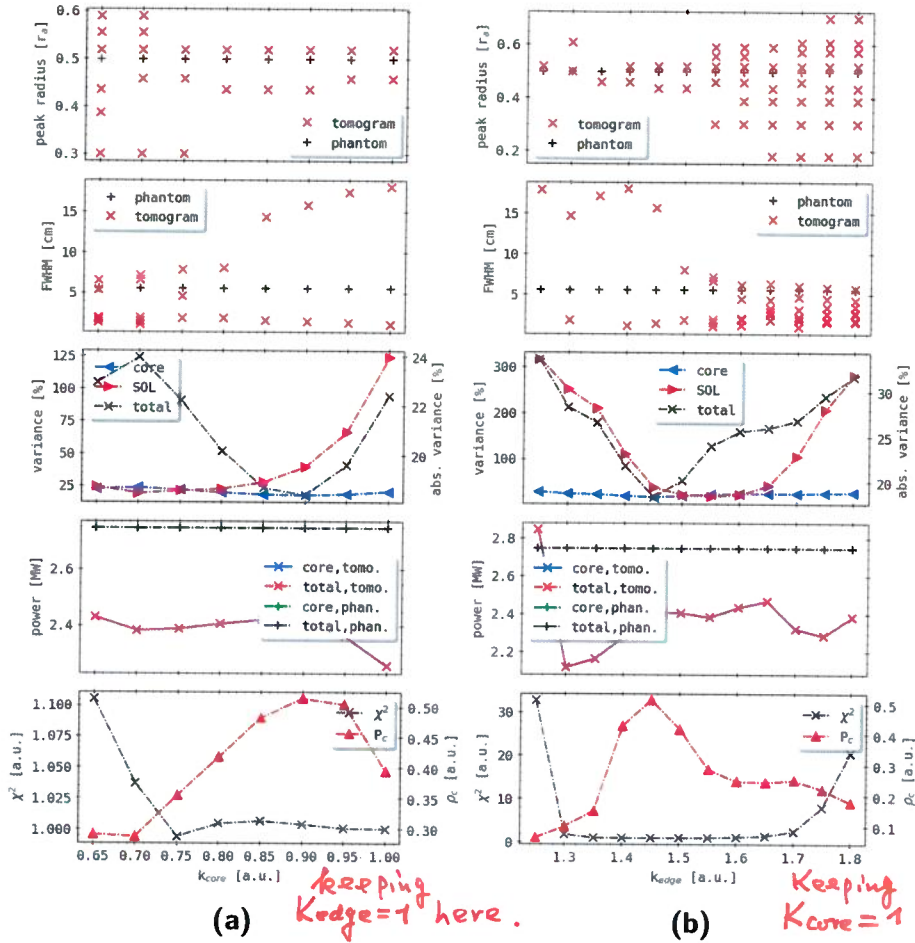


Figure 5.36.: MFR scan of phantom radiation distribution consisting of an isotropic ring at $0.5r_a$ with 0.1 m FWHM. (a) Core and (b) edge RDA coefficients are varied independently. In both, top to bottom: radial position of the maximum, FWHM, MSD for core, SOL and in total, total and core integrated 2D powers and fitness scales χ^2 and Pearson coefficient ρ_c .

← Do you
mean this?
How about
keeping
at
 $K_{edge} < 1$?

integrated, two-dimensional power from equation (5.16) and finally the fitness factor χ^2 and Pearson coefficient ρ_c in the bottom figure. Each plot contains of course two sets of lines for phantom and tomogram separately, except the very last in which the quantities are derived from both together.

If applicable, multiple abscissa are indicated where the order of magnitude between the profiles is distinctly different.

At the top, the input radiation distributions maximum brightness radial location is obviously constant at $0.5r_a$ across both k_{ani} spectra. For $k_{\text{core}} \leq 0.75$ a. u. in column **(a)**, the tomogram yields at least three individual peaks both inside and outside the respective target radius, though one data point can be found here very close at $0.52r_a$. Overall, features between $0.3 - 0.59r_a$ are presented, while beyond $k_{\text{core}} \geq 0.8$ a. u. only two extremes are shown in the tomogram relatively constantly in $0.55r_a$ and $0.45 - 0.5r_a$. When varying the SOL regularisation parameter in **(b)**, for $k_{\text{edge}} = 1.25$ a. u. a singular maximum is located nearly precisely where the original ring is in the phantom, i.e. in $0.052r_a$. In $k_{\text{edge}} = 1.3$ a. u., this peak is at the aforementioned position and a secondary point is added in $0.6r_a$, after which in 1.35 a. u. again only one extremum in $0.47r_a$ follows. Beyond, count and spread of the tomogram features increases continuously, until for $k_{\text{edge}} = 1.8$ a. u. eight individual maxima are produced in the tomogram between $0.18 - 0.7r_a$, though still and throughout on is presented reliably in $0.52r_a$. Newly appearing peaks can be found consistently at that radius for larger k_{edge} than where they first are noted.

In the second line of plots, the corresponding FWHM of the phantom is 5.5 cm. The same respective number of data points is shown across the k_{core} and k_{edge} spectra as above, though this representation does not link the individual features explicitly across the images. In the core regularisation weight variation, for lower values $k_{\text{core}} \leq 0.8$ a. u. the grouping is significantly closer around the target width, even for the increased number of maxima shown, i.e. 1.5–8 cm. Beyond, the reduced amount of peaks is increasingly spread out more in their width to 1–18 cm for larger k_{core} . On the other side for varying k_{edge} , the opposite behaviour is presented, where for fewer features and smaller edge regularisation weights $k_{\text{edge}} \leq 1.45$ a. u., the distribution of data points is far wider at 1.5–18 cm. For higher k_{edge} , this is similarly reduced to 1–8 cm at simultaneously growing numbers of maxima.

In the next row of plots, the integrated relative variance calculated by equation (5.14) is shown, individually separated for the SOL, core and an absolute value across the entire, triangular plane reconstruction domain. On the left, until $k_{\text{core}} = 0.8$ a. u., the MSD in- and outside the separatrix are relatively constant around 25 % with minor deviation. For larger weighting parameters, the SOL discrepancy increases parabolic to 125 % in $k_{\text{core}} = 1$ a. u. while

5.3. Phantom Radiation Profiles

the core error remains low and even occasionally drops below 25 %. The total variance is the integrated sum of the prior two and yields 20–24 % up until 0.8 a. u. across which it steadily falls to 18.5 % in 0.9 a. u. and then becomes dominated by the SOL divergence, i.e. parabolically growing to 22.5 %. Across the spectrum of k_{edge} on the right, the core MSD is mostly constant around 30 %. Absolute and SOL deviation are similar in profile, though differ greatly in value until $k_{\text{edge}} = 14.5\text{--}15$ a. u.: starting at a maximum 320 % and 33.5 %, they continuously decrease until 30 % and 19 % respectively. The SOL error remains low as long as $k_{\text{edge}} = 1.65$ a. u., after which a near linear increase to 280 % is shown. Accordingly, the absolute deviance also rises immediately again and slightly plateaus around 1.6 a. u. and 25 % and then climbs to 31.5 % for $k_{\text{edge}} = 1.8$ a. u..

In the fourth line of images, the integrated power of the phantom from the core and conclusively also in total is 2.75 MW. Between $k_{\text{core}} = 0.65\text{--}1.0$ a. u., the tomograms $P_{\text{rad},2D}$ from in- and outside the LCFS does not change drastically and yields 2.25–2.44 MW, with most reconstructions producing close to 2.4 MW. On the right, for $k_{\text{edge}} = 1.25\text{--}1.3$ a. u. this value drops from 2.85–2.12 MW and then also increases to 2.4 MW in 1.45 a. u., around which it deviates across the rest of the spectrum by ± 0.1 MW. Core and total radiation power are equal here too.

The final set of plots presents the two aforementioned quality gauges fitness factor χ^2 and Pearson coefficient ρ_c , similarly with split abscissa for each number individually. Between $k_{\text{core}} = 0.65\text{--}0.75$ a. u., χ^2 decreases from 1.105–0.995 a. u. and after equals to 1 a. u. across the rest of the spectrum. The Pearson coefficient yields 0.29 a. u. for lower values and near linearly grows to its maximum 0.51 a. u. in 0.9 a. u. before dropping again to 0.39 a. u. for k_{core} unity. A comparable image is shown on the right, though the χ^2 decrease is absolutely larger from 33–2 a. u. and its plateau finalized by a parabolic rise to 21 a. u. towards $k_{\text{edge}} = 1.8$ a. u. The ρ_c maximum of 0.51 a. u. is now in 1.45 a. u. and is concluded by a small plateau between 1.55–1.75 a. u. around 0.25 a. u.

Focusing on one column of plots at a time, the vertical alignment for individual k_{ani} of features in the respective plots reveals an intuitive and characteristic behaviour across that spectrum. On the left, the fitness is closest to unity, while the Pearson coefficient is largest for $k_{\text{core}} = 0.9\text{--}0.95$ a. u.. At the same time, the cumulative core, SOL and absolute deviation in total are lowest and the error in integrated power is relatively constant at around

inside the separatrix does so from 3.5 MW to a shallow and plateau-like maximum of 6.5 MW in $0.8r_a$ before decreasing again more quickly to 3 MW in the end.

Finally, the very last figure in the right column of figure 5.37, the fitness factor and Pearson coefficient for the variation and reconstruction of the double concentric brightness ring combination are presented. The prior is calculated in a narrow band of $\chi^2 = 0.992\text{--}1.006$ a. u., indicating strong agreement between phantom and tomogram, however the profile shown has a pronounced minimum below unity of 0.992 a. u. in $0.8r_a$. For inner ring radii below and above, values at or higher than 1.0 a. u. are produced and below $0.65r_a$ or above $0.9r_a$ even more than 1.003 a. u.. Similarly, ρ_c is close to unity and within a smaller range of 0.895–0.99 a. u.. From 0.94 a. u., a parabolic decay to a minimum of 0.895 a. u. in $0.6r_a$ is followed by continuous increase to the maximum of 0.99 a. u. in $0.9r_a$ and an insignificantly smaller, minor plateau at 0.955 a. u. beyond.

? For the given configuration of $k_{\text{ani}} = \{2, 2\}$ and ring positions, i.e. a fixed larger concentric structure at $1.05r_a$ and a variable smaller inside, the applied algorithm yields generally acceptable results. In contrast to on the left, no significant deviations in reconstruction quality across the radial spectrum of the inner ring can be observed. Location and shape of the rings are consistently and accurately represented, while the overall power is congruent throughout. However, both absolute variance and fitness factor χ^2 indicate a worse match of the tomogram at an inner radius of $0.8r_a$, though beyond and hence for a smaller distance between the profiles the error decreases and χ^2 gets closer to unity again. On the other hand, ρ_c is smallest for the greater radial differences and closest to 1 a. u. in that range at and beyond $0.8r_a$. Coincidentally and trivially, the SOL deviation also peaks here and the individual peak detection eventually fails. Conclusively, the given radiation structures are reconstructed with the presented configuration nearly uniformly well, except a threshold value and negligible spacings. The prior appears to, judging from the shown results, not correlate with known characteristic of this system.

Anisotropic Island Combinations

Of much greater relevance towards the reconstruction of potentially more complex and anisotropic experimental data is the individual k_{core} and k_{edge}

numbers. With respect to the first plots of extremes location and shape, the largest diameter have to be excluded or at least treated differently in terms of anisotropic weighting and statistic evaluation, further supporting the optimum up until that range.

Based off of that knowledge, the results plotted in the right column of images in figure 5.37:(b) can be interpreted much easier now. At the top, the outside and variable inside brightness ring are clearly distinguishable in $1.05r_a$ and with increasing radial position from $0.4 - 1.0r_a$, respectively. At the very outside for the last variation, the algorithm only yields one maximum at the aforementioned location, indicating a merging of the previous two. Across the spectrum, the reconstructed profiles produce overall congruent or at least very similar values up until $0.8r_a$. Beyond that, the points begin to converge and already for an inside ring radius of $0.95r_a$ only one maximum is found in the tomograms, though its position aligns with the phantom.

The FWHM below shows a nearly constant 4–7 cm in a varying number of points, i.e. one or two due to the similarly configured rings, up to $0.8r_a$ of the inside ring from the phantom. For larger radii of the latter and a decreased distance between the two, the individual points split and are now decreasing linearly from 13–8 cm and 3–1 cm, while at congruence of the rings the smaller width vanishes. Results from the tomograms are overall in agreement with a small tendency to overestimating the target FWHM by 1–2 cm, although occasionally one of the two points might match. At $0.8r_a$ and onward, the indicated profile shapes are split again, where the larger is now already at 19 cm and only two smaller diameters can be found before null. At those radii, similar or smaller deviations are shown.

In the core and SOL, the relative variance is much smaller than before, within 2.5–32.5 % overall, while the absolute error is within the same range of up to 11.9 %. Deviations in the core increase nearly linearly with the radius of the inner ring from 10–32 %, before decreasing at the last position to 28 %. At the same time, the core variance is almost constant around 5–6 % with a small, minor maximum at $0.8r_a$ of 10 %. As a combination of the latter two, the total error across the profile grows steadily from 6.5–9 % in $0.75r_a$, until peaking sharply in $0.8r_a$ and dropping just as quickly to 7.5 cm and finally 5.5 % at the last variation.

Across the radial spectrum, the tomograms and phantoms core and absolute integrated power values are, within a margin of <0.25 MW in congruence. The latter increases linearly from 10–14 MW, though the total emission from

Due to the shape of the artificial distribution, the SOL error is beyond 6000 % at the smallest diameter, where essentially no emissivity is placed in the phantom and small deviations in the reconstruction immediately lead to very large relative discrepancies. This then parabolically decays with increasing ring radius. Simultaneously in the core, comparatively much smaller values are presented, though the abscissa scale and difference in order of magnitude does not allow for a more detailed assessment. Only at $1.2r_a$ a noticeable and still very large error of ~ 500 % can be found inside the LCFS. On the other side, the absolute variance yields more comprehensible results, with values between 2.5–12.5 %. For the innermost ring, the total discrepancy is largest with 12.2 % and continuously decreases with larger radii, though a small plateau around 10 % and $0.7r_a$ – $1r_a$ precedes a sharper drop towards the edge of the spectrum, where the points show a strong variability. In $1.2r_a$, the absolute error increases again sporadically to 7.5 % before reaching the minimum at the edge of the domain.

Integrated power values of the two-dimensional distributions are generally in very good agreement throughout the radial variations, particularly the absolute $P_{\text{rad},2D}$ is basically congruent between the tomogram and phantom. The latter grows near linearly from 2.5 MW to 9.5 MW in $1.1r_a$ and quickly drops to 0.75 MW at $1.3r_a$ from there. Until $0.8r_a$ the total amount of emissivity is almost entirely focused in the core, though beyond this correlation obviously degrades and from $0.9r_a$ decays fast to null, where also the two profiles yields slightly different results with ± 0.5 MW deviation.

The very last plot on the left shows that the fitness factor χ^2 is nearly constant at ~ 1 a. u. until a ring radius of $0.9r_a$, while the Pearson coefficient ρ_c presents an at first steep and then staggered increase in that range from 0.79–0.89 a. u.. For larger diameter, the latter grows continuously to 0.98 a. u. and χ^2 decreases rapidly inversely parabolic to 0.75 a. u. in $1.2r_a$ and then null at the edge.

All the above indicates that the reconstruction of an isotropic, radially thin radiation distribution for a given set of regularisation parameters assuming such performs best for a concentrated emissivity in the range of 0.9 – $1.1r_a$, i.e. in and around the LCFS. Although fitness and Pearson coefficient both produce maxima at opposite ends of the spectrum and are not at unity at those radii, they yield sufficient values indicating good overall agreement between the forward and two-dimensional profiles. This is also true for the presented individual and absolute variance, as well as all the shown power

5.3. Phantom Radiation Profiles

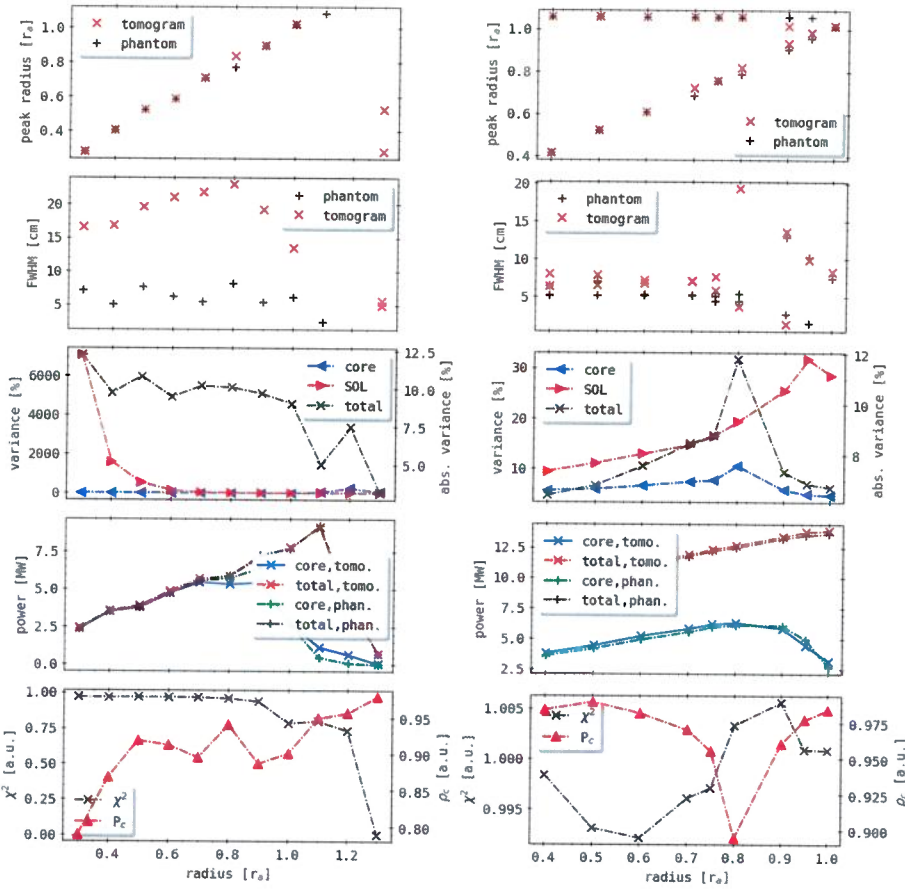


Figure 5.37.: MFR scan of phantom images consisting of (a) one or (b) two concentric, isotropic, equally bright rings. In (b) only the inside rings' and in (a) both rings' radii have been varied, while the same RDA coefficients $k_{\text{core}}, k_{\text{edge}} = \{2, 2\}$ are used throughout. The layout of the results is similar to figure 5.36.

again due to the discrepancy between continuous and discrete mappings. Towards the edge beyond r_a , this relation degrades as no peaks are found in the target profile and the tomogram shows similar and almost identical widths for both extremes around 5 cm. With increasing radius, the width in the tomogram grows slightly, though drops as quick closer to the LCFS.

0.2 MW. However, though the peak localisations are comparatively improved for those values, the FWHM deviate greatly here with respect to the lower k_{core} . Similarly, on the right, the lowest individual and total two-dimensional variance is found for $k_{\text{edge}} = 1.45 \text{ a. u.}$. At the same time, ρ_c is largest and χ^2 is very close to unity, while the reconstructed structures are radially close to the location of the input profile. The corresponding widths are also in stark contrast here and $P_{\text{rad},2D}$ yields again an equivalent error, though a singular outlier for a smaller k_{edge} does not align with those observations. Conclusively, for this kind of simple and symmetric radiation distribution, there do exist ideal k_{core} and k_{edge} , individually given a fixed counterpart. In this case, the quality parameters shown are largely in strong agreement across the spectra and no significant characteristic is found that is in contradiction. However, a large drawback of this particular approach is the large parameter range that has not been explored by this relatively expensive method. For only one phantom image, a small spectrum of anisotropic weighting coefficients has been evaluated separately. For N the number of variations in this small window, one would have to perform at least $N \times N - 2N$ more reconstructions to find a definitive answer to what the actual optimum k_{ani} profile is. Another possible ansatz is the variation of the artificial brightness distribution for constant reconstruction settings, i.e. changing the radius of the ring in the previous data set instead of k_{core} and k_{edge} each.

This procedure has been applied in figure 5.37, where two similar types of previously presented, simple phantom radiation profiles have been varied and conclusively reconstructed using the Minimum Fisher algorithm for a set of constant $k_{\text{ani}} = \{2, 2\}$. The same set of quantities as in figure 5.36 have been measured for each of the results. In (a), the radial position of a magnetic axis concentric, isotropic singular thin, bright ring is altered between $0.35r_a - 1.3r_a$, while at the two very last iterations the actual maximum emissivity in the phantom is close to or outside the regularisation domain due to the aforementioned mapping to discrete cells. This inevitably leads to missing data points in the first plot of maximum brightness locations at the right edge of the spectrum, however the tomogram finds two individual peaks at a target radius of $1.3r_a$ in $0.28r_a$ and $0.55r_a$. Otherwise, the results are congruent except for in $0.8r_a$ where the reconstructed image yields a ring of slightly larger diameter. In contrast, the FWHM values differ significantly and nearly constantly, as the tomograms produce distributions with around 15–25 cm thickness and the phantom with 5–7 cm. The latter variability is

Why?

5.3. Phantom Radiation Profiles

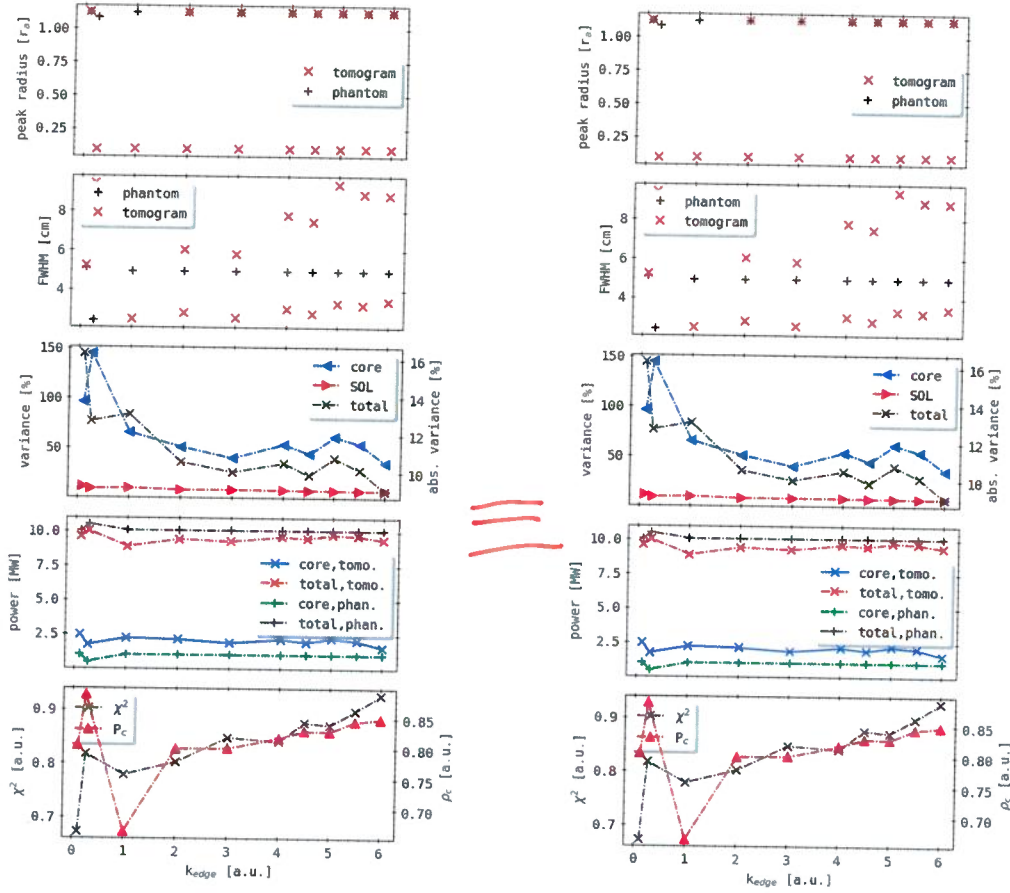


Figure 5.38.: MFR scan of a phantom image consisting of *up-down* symmetrical chain of island-like radiation spots at $1.1r_a$ of 0.1 m FWHM (exemplary artificial profile can be found in figure 5.30). **(a)** Core and **(b)** edge RDA coefficients have been varied independently. The layout of the results is similar to figure 5.36.

variation for an *island chain-like* artificial profile like in figure 5.38. Here, a ring of five island-like structures are placed, like before in figure 5.36 with one less feature, around the triangular at a radius of $1.1r_a$ and FWHM of 0.1 m

Foo.

?

53°

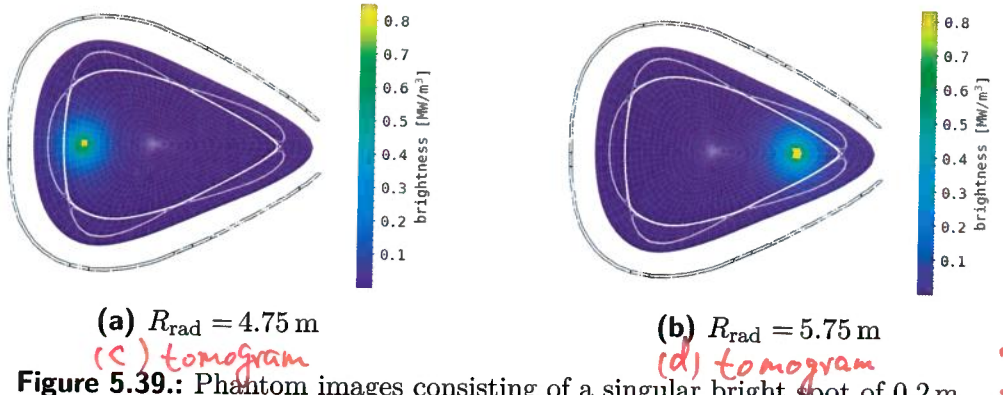


Figure 5.39.: Phantom images consisting of a singular bright spot of 0.2 m FWHM - (a) inboard and (b) outboard anisotropies.

Composite Phantom Images

At last, a less complex than before, though more intricate to reconstruct artificial radiation distribution is simultaneously introduced and MFR scanned by varying $k_{\text{core}} = \{0.4, 1\}$ while keeping $k_{\text{edge}}=1$ in figure 5.40. In figure 5.39:(a), a singular, large bright spot with omnidirectional Gaussian profile and 0.2 m FWHM is placed in $z = 0$ and major radius $R_{\text{rad}} = 4.75 \text{ m}$. Its central, maximum brightness is 0.85 MW/m^3 .

Kedge=? —

In the tomograms, for $k_{\text{core}} \leq 0.75$ a. u. multiple, erroneous maxima are found in $0.62r_a$, $0.46r_a$ and one in $0.52r_a$, while the target value from the phantom is $0.41r_a$. However, across the spectrum, similarly close points are produced in $0.34r_a$ and then for $k_{\text{core}} \geq 0.7$ a. u. in $0.37r_a$. The corresponding FWHM of the artificial distribution is a constant 14 cm. At the lower $k_{\text{core}} \leq 0.75$ a. u., the majority of the faulty results from above yield <5 cm and as low as 1.5 cm. Across the spectrum, one of the peaks is accounted for by oscillating values between 6–9 cm, where the minimum is in $k_{\text{core}} = 0.85$ a. u. and the maximum in 0.95 a. u..

The relative variance in the core is nearly constant with 10–13 % until a small peak in $k_{\text{core}} = 1$ a. u. of 15 %. On the other hand, the SOL error is significantly larger and varies strongly, with a steady decay from 60 % to 35 % in $0.95r_a$, a minor plateau in-between and a conclusive maximum of 65 %. Obviously the shape of the absolute deviation is dominated by the outside error, hence the alike profile in the range of 13.5 % in 0.6 a. u. and 9 % in 0.95 a. u. It is terminated by a peak of 15 %.

5.3. Phantom Radiation Profiles

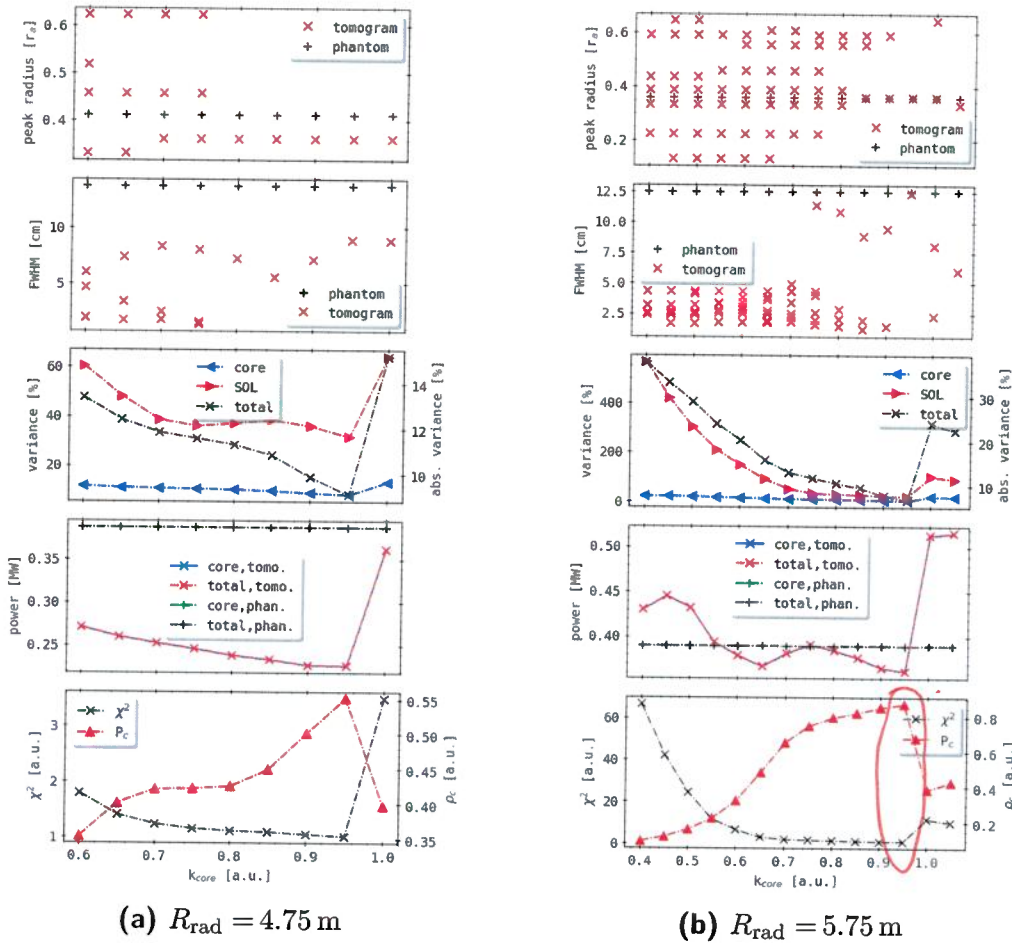


Figure 5.40.: Reconstruction scan for the corresponding phantom images in figure 5.39, a singular bright spot of 0.2 m FWHM - (a) inboard and (b) outboard anisotropies. In both, k_{core} has been varied in the same range. The layout of the results is similar to figure 5.36.

The best k_{core} and k_{edge}

values are ...

In the phantom, the total integrated power from the two-dimensional distribution is entirely represented by the core and constant at 0.39 MW. Results from the phantom also show congruence between the inside the separatrix and absolute calculated values throughout the k_{core} spectrum. Beginning in 0.27 MW, both linearly decay to 0.23 MW in 0.95 a.u. The final data point yields a drastic increase to 0.36 MW. Finally, the fitness χ^2 similarly

How about
 $k_{\text{core}} = 0.95$?
 Here, $P_c \approx 1$
 $\chi^2 \approx 1$,

decreases with larger k_{core} from 1.9 a. u. to 1 a. u., followed by a sharp growth to 3.6 a. u. Curiously, the Pearson coefficient ρ_c indicates the opposite behaviour, i.e. increasing from 1 a. u. to a small plateau in 1.9 a. u. around $k_{\text{core}} = 0.75$ a. u. and then quickly to 3.5 a. u. before the conclusive drop to 1.5 a. u.

The k_{core} scan of the second tomogram in figure 5.39:(b) is shown in figure 5.40:(b). Here, the multiplicity and spread of the erroneous and individually reconstructed peaks is greatly increased compared to before. The input profile yields a value of $0.35r_a$. Until 0.8 a. u., six to seven maxima are found between $0.125r_a - 0.65r_a$, while throughout that spectrum the majority of features are consistently placed in $\{0.225, 0.33, 0.43, 0.59\} r_a$ and a few in $\{0.12, 0.42, 0.55, 0.625\} r_a$. Beyond, the number of points is decreased noticeably to three at most, even less for larger k_{core} and one is placed in location of the target structure. Concurrently, the representation in the plot of FWHM shows equally many points, with decreasing spread and amount with increasing inside anisotropy weighting. The bulk of the results is found for 2–5 cm and concentrated around 3 cm. From 0.75 a. u. on, singular points can be found >7.5 cm, descending with larger k_{core} from 11.5 cm. In 0.95 a. u., one result matches the target exactly.

Integrated error values from the SOL are very large and decrease parabolically from 460 % to <50 % in 0.95 a. u., then rise to 90–100 a. u.. Since the core variance is comparatively constant around 25 %, with a minor increment to 40 % in a similar range, the total discrepancy of 16–38 % throughout the k_{core} variation is dominated by the difference in SOL emissivity. The conclusive step in >0.95 a. u. is significantly more pronounced here in relation to the profile to 23 %.

From a constant, integrated power of 0.39 MW in the phantom distribution, the tomograms yield 0.36–0.44 MW up to $k_{\text{core}} = 0.95$ a. u. in an oscillating manner with a slight downward trend. Throughout, core and absolute values are identical, even in the large spike for ≥ 0.95 a. u. to 0.51 MW.

Fitness factor and Pearson coefficient both indicate an optimal reconstruction within the presented interval in $k_{\text{core}} = 0.95$ a. u., where χ^2 and ρ_c are closest to unity, i.e. ~ 1.5 a. u. and 0.87 a. u. respectively. The prior decays parabolically from 68 a. u., while the latter increases from null gradually, with a small steep portion around 0.65 a. u. and shallow end towards its aforementioned maximum. They decrease in quality afterwards, i.e. grow strongly again or drop sharply correspondingly.

The final k_{ani} variation results for the above, highly anisotropic phantom radiation distribution evidently pronounce a strong optimum within the limited range. For such clearly separated and singular emissivity features inside the separatrix, a factor of $k_{\text{core}} = 0.95$ a. u. yields adequate tomographic reconstructions in regard to the quantitative analysis. Given the generality of the approach and underlying artificial images, one expects similar behaviour with larger scale asymmetric features in superimposed profiles or experimental data. However, the variance of the quality of results in this small window somewhat mitigates the significance of said conclusions, since minor differences in either localisation, shape or k_{ani} may lead to severe changes in the tomogram. The asymmetry in reconstruction parameter profiles around the optimum is of particular concern for the exploration of non-artificial radiation data. Furthermore, the same is true for the noticeable discrepancies between the in- and outboard anisotropy and hence the images presented in the left and right column of figure 5.40, which can be trivially attributed to the geometry of multicamera bolometer system.

**Conclusion
and
remarks.**

This concludes the efforts of benchmarking and evaluating the *Minimum Fisher regularisation* algorithm with *radially dependent anisotropy* weighting with a large set of deliberately designed and, albeit small scale, statistically varied set of phantom emissivity distributions as input. The propagation and their level of impact of errors in the underlying line-of-sight geometry has also been measured. Due to the nature of the multidimensional parameter dependency of the quality of MFR results, variations of such in an attempt to find optimal configurations or sets of coefficients like k_{ani} have proven difficult. However, for the select set of artificial radiation profiles and hence conceptually it was shown that there does exist an ideal combination of MFR parameters for a given emissivity distribution. As per design, there it was also found that regularisation weights $k > 1$ correspond to isotropic and coefficients $k < 1$ to anisotropic brightness profiles with improved quality factors for fitness, χ^2 and two-dimensional correlation, ρ_c .

Respective setups of symmetrical phantom images with reconstruction weights favouring smooth distributions have indicated geometric biases towards the individual camera apertures location, i.e. areas of increased lines-of-sight coverage along the lower part of the separatrix, inboard side and at the outboard tip of the triangular plane. Furthermore, from the perspective of the up-down symmetrically designed horizontal bolometer camera, this and the intrinsic

tilt of the detector fan leads to a systematic and intrinsic asymmetry in the produced forward and backward calculated radiation powers. Individual case testing with deliberately symmetric-asymmetric superimposed artificial profiles presented results of strongly divergent qualities, further underlining the previous assessment. Simultaneously, variation in k_{ani} highlighted significant discrepancies between the one- and two-dimensional pictures, hinting at independent qualitative developments in both.

Experimentally motivated phantom emissivity distributions, i.e. combined smooth, symmetric core and anisotropic SOL profiles mimicking hotspots in place of the magnetic islands prove to be a particular challenge for the MFR. With respect to the structure and localisation of the outside features, the regularisation weight optimisation is especially important. Addition of a hypothetical, inboard located horizontal camera has provided noticeable qualitative improvement for this type of phantom, suggesting and supporting the demand for an extension of the existing multicamera bolometer system. Finally, occlusion of the anisotropic profile on the inside by a homogenous, similarly bright ring yields promising results towards the inversion of experimental data compared to the initial case.

The previously introduced potential discrepancy between the assumed and actual *in-situ* geometry of the bolometer camera array was tested and evaluated in regard to its impact as an unknown, systematic error to the forward and backward calculated line integrated signals. Alteration of the aforementioned variance produces characteristic divergence of corresponding orientation in the MFR tomograms and profiles. However, that effect is indistinguishable from the various other variabilities in the reconstruction and of no such noticeable magnitude. This then provides an additional uncertainty to be taken into account when evaluating actual measurement data.

Iteration in k_{ani} and thorough quantitative analysis for principle emissivity shapes or combinations thereof was performed. Significant anti-/correlation between the individual variance, fitness and Pearson coefficients underlined the previously, only in isolated cases presented discrepancy to the subjectively perceived tomogram quality. The shown spectra also visually underline the proposed optima of MFR parameters through structural congruence or extremes in qualitative numbers.

which one? Their value?

5.4. Tomography of Experimental Data

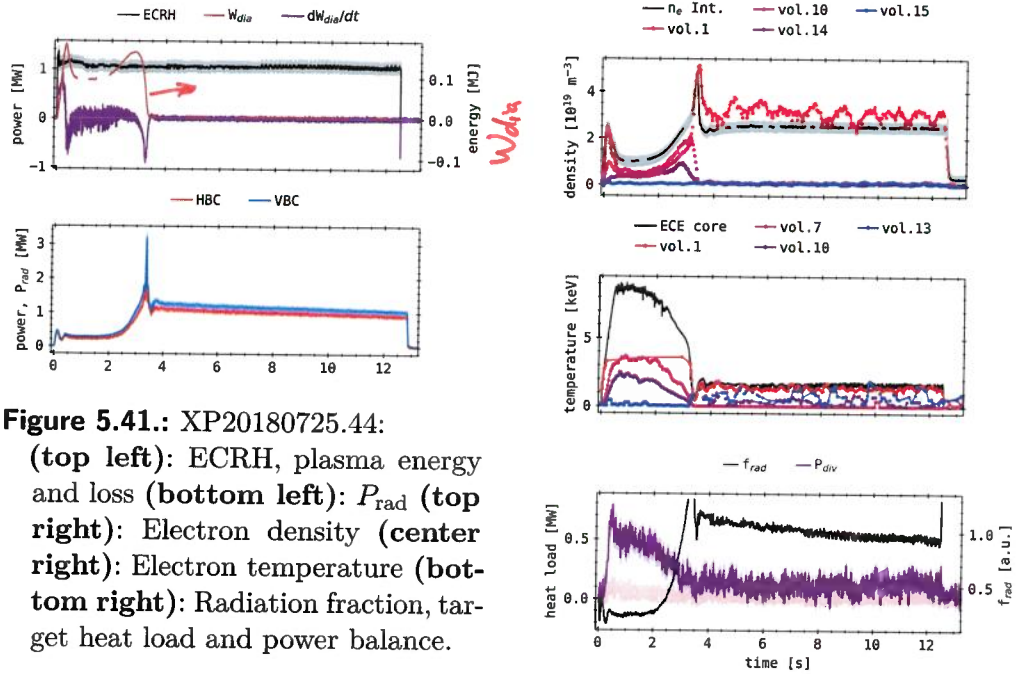
At last, after finalizing the benchmarking of the core MFR algorithm with an extensive set of artificial radiation distributions, regularisation weight coefficients, variations and input geometries, one will proceed to perform tomography with experimentally measured data. However, due to the limited scope of this work, the set of experiments investigated in this section will also be focused on discernable and reasonable features in their respective tomographic reconstructions of adequate fitness and k_{ani} . The latter are established by finding a χ^2 closest to unity for a given optimum set of weighting parameters that is within a sufficiently, yet restrictively extended interval in line with the experiences and statistics of the previous segment. Introduction and approach to the below data is of exemplary character and will be done so with respect to the corresponding central plasma parameters. For sake of comprehensibility and manageability, presentation of the individual $P_{\text{rad}(2D)}$, χ^2 and forward and backward calculated detector signal profiles will be omitted. Their relevance towards the evaluation of this nature is limited, though they are recorded regardless and employed later on in an overarching comparison for all and per discharge experimental and phantom reconstructions.

XP20180725.44

The ~~central~~ plasma parameters for experiment *XP20180725.44* are shown in figure 5.41, including ECRH, HBC and VBC radiation power P_{rad} , diamagnetic energy W_{dia} , its temporal derivative, a selection of *Thomson scattering* LOS volumes and line integrated dispersion interferometry for electron density, as well as electron cyclotron emission temperature measurements. Thereof derived radiation fraction f_{rad} and integrated divertor heat load are plotted separately. This was partially already introduced and discussed in figure 2.27, only the electron quantities have been added in this case. Here, the magnetic configuration is that of a high mirror field (*KJM*), hence the slightly altered shape of the triangular plane, island structure, reconstruction domain and subsequent pixel grid.

After an initial smaller spike in n_e after plasma startup to up to 2.5 m^{-3} in 0.2 s, with lesser pronounced maxima and absolute values the further radially outside the LOS volumes are located, the density decays again and then

? $2.5 \cdot 10^{19} \text{ m}^{-3}$



parabolically increases to 5 J/m^3 in 3 s. The latter shows a similar behaviour, though the outermost measurements rise earlier and may not even yield a peak at all. Afterwards, from 3–12.5 s only the innermost and interferometer data show significant n_e values around $2.5\text{--}3.75 \text{ J/m}^3$ and all other volumes drop to null.

unit !

The electron temperature similarly has a strong increase within the first 0.5 s to up to 9 keV in the core and less the further outward the LOS volume is located, i.e. 2.5–3.8 keV. The outermost volume no. 13 does not increase before 3.2 s and is essentially null until then. Between 0.5–3.4, the temperature first gradually and then rapidly decreases to nearly zero - the innermost TS volume however yields no data points in that interval. Successively, T_e grows slightly and remains relatively constant around 1.9 keV until 12.5 s, while the outside volumes show lower temperatures and vary significantly within that range, though volume no. seven remains null and the profiles of no. ten and 13 might be within their respective uncertainty intervals, given the offset after discharge termination >12.5 s.

The radiation fraction is cut off at $f_{\text{rad}} > 1.4 \text{ a.u.}$ and generally follows the

5.4. Tomography of Experimental Data

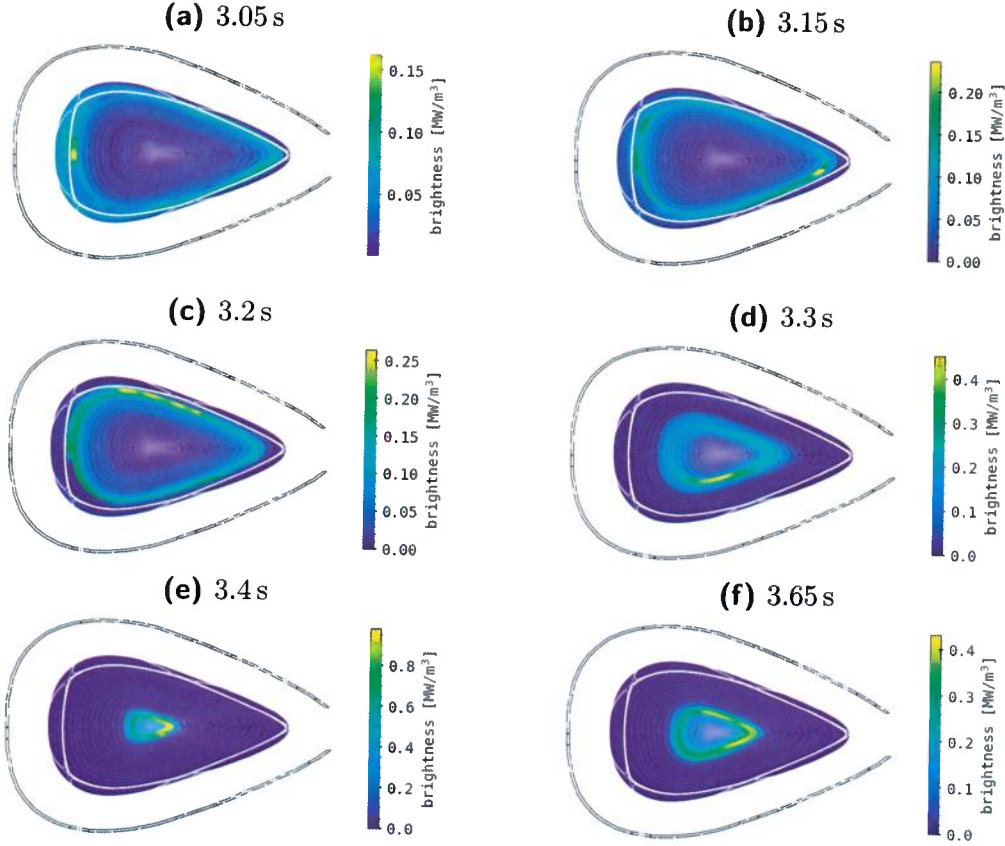


Figure 5.42.: XP20180725.44:

Tomograms for the above discharge on a $1.25 r_a$ inflated grid with $n_r \times n_\theta = 20 \times 150$ and *KJM* high mirror magnetic configuration. RDA parameters applied here are $k_{\text{core}}, k_{\text{edge}} = \{2, 0.25\}$ with $N_T = 15$ and $N_S = 2$. Central experiment parameters can be found in figure 5.41.

shape of both cameras P_{rad} profiles, since the ECRH can be considered constant throughout the experiment. Hence, the plot is broken up between 3.2–3.4 s, where the radiation power eclipses the heating by a factor of 3.2 and then also slowly decreases, which is concluded again by a spike beyond the spectrum due to the plasma and radiative decay after the shutdown of the microwave heating.

In figure 5.42, an excerpt of six points in time just before and across the

Chapter 5. Two-dimensional radiation inversion

the time point, t=3.4s, with P_{rad} maximum

pronounced global maximum in 3.4 s from the multicamera, bolometric measurement is reconstructed using the same set of $k_{\text{ani}} = \{2, 0.25\}$ and secondary coefficients $N_T = 15$ and $N_S = 2$ (see section 5.1.1). This configuration strongly favours smooth and isotropic emissivity profiles inside the core up to two cells close to the separatrix and therefore more anisotropic structures beyond until the edge of the domain.

The first tomogram in (a) for $t = 3.05$ s shows a relatively even and smooth, shallow profile of $\sim 0.12 \text{ MW/m}^3$ along the LCFS of increased width. On the inboard side and towards the lower X-point, this is moved further inward and a distinct maximum can be found around $z = 0$ with 0.16 MW/m^3 , while the correspond island is also slightly brighter than the rest. The core is mostly dark with an emissivity $< 0.05 \text{ MW/m}^3$.

In (b) for $t = 3.15$ s, this somewhat smooth and thin ring has shifted radially inwards towards the magnetic axis. A decrease in radius by about two cells or $\sim 0.05r_a$ is accompanied by poloidal translation of the maximum emissivity of 0.23 MW/m^3 closer to the HBCm aperture, adjacent to the lower outboard magnetic island. The inboard side of the profile is still noticeably brighter with 0.17 MW/m^3 compared to the rest at 0.13 MW/m^3 . At $t = 3.2$ s in (c), the distribution has shrunk even further, however not homogeneously but rather by establishing a more pronounced edge towards the now entirely radiation-less SOL and separatrix area. Hence, the ring brightness grows slightly overall to $0.18\text{--}0.2 \text{ MW/m}^3$ and the peak power of 0.26 MW/m^3 can be found closest to the midplane, upper X-point with minor substructures and an increased poloidal width.

For $t = 3.3$ s, tomogram (d) shows a now significantly, radially smaller profile of very smooth emissivity, besides the maximum towards the lower inboard magnetic island. The latter, now smaller again yields 0.42 MW/m^3 and the, to $0.3r_a$ widened ring 0.3 MW/m^3 while its center and outside area remain without noticeable radiation.

Coincidental with the peak in P_{rad} , the core n_e measurements and dW_{dia}/dt , the second to last reconstruction for $t = 3.4$ s in (e) shows the smallest brightness profile at only a radius of $0.2r_{ixa}$, also featuring the highest overall and maximum emissivity of $0.7\text{--}0.97 \text{ MW/m}^3$. The highest radiation density is found towards the tip of the triangle-shaped plane, though due to the reduced size of the distribution this expands to nearly half the circumference of the latter. Still, this small ring appears slightly hollowed like before and otherwise smooth. Radial width or decay of said feature is comparable to

why do you
use this
set?
Please clar-
it.

5.4. Tomography of Experimental Data

before, given the significantly different ratio between size and shape. Finally, at the equilibrated plateau shortly after that peak in $t = 3.65$ s, tomogram (f) presents again a larger brightness profile with a radius of $\sim 0.3r_a$, with a similar structure but only less than half the intensity of the previous reconstruction, i.e. $0.3\text{--}4.3 \text{ MW/m}^3$. Width, poloidal smoothness and hollowness are also nearly congruent to the prior. Like in the preceding three tomograms, no radiation is placed outside the edge of the distinctly confined distribution.

This first exemplary discharge in figure 5.41 and its corresponding, selective MFR of experimental data in figure 5.42 yield plausible, albeit qualitative correlations. The behaviour of the two-dimensional radiation profiles corresponds well with the indicated plasma density and its temporal evolution, particularly the intrinsic discrepancy between the outer and inner LOS volumes. The same is true for the reduction and centralization of T_e during that time, coinciding with an increase and narrowing in the tomogram radiation powers for a constant input microwave heating and negligible plasma stored energy. Furthermore, with respect to the total P_{rad} of both cameras, the quantitative character of the brightness distribution across the selected points in time is also well-supported. Given the shape and structure of the reconstructed profiles, the applied anisotropic regularisation weight coefficients $k_{\text{ani}} = \{2, 0.25\}$, $N_T = 15$ and $N_S = 2$ produced adequate results that align with the established phantom image benchmarks.

(See section ?)

XP20180809.13

The next exemplary discharge XP20180809.13 and its central plasma parameters are presented in figure 5.43. It is particularly characterised by a constant heating power P_{ECRH} , generally very low radiation fraction $f_{\text{rad}} \leq 0.25$ a. u. and two distinct events that lead noticeable, large spikes in radiative power loss P_{rad} . These are caused by the injection of tertiary impurities through the ablation of metal ^w particles by a *Laser Blow-Off* (LBO) system - a concentrated, high power laser beam superheats, ablates and ejects from plasma-side coated glass tiles into the SOL. The injected amount is relatively small, though possible charge states increased, hence the negligible or small impact on W_{dia} and the electron density and temperature. The input P_{ECRH} is, after an initial step to 2 MW before 0.25 s and subsequent decay from 3.5 MW, set constant at 2.6 MW. Correspondingly, the plasma

time traces of plasma

→ adding Ref.

{Th. Wagnor, 2016
Rev. Sci. Instr.]

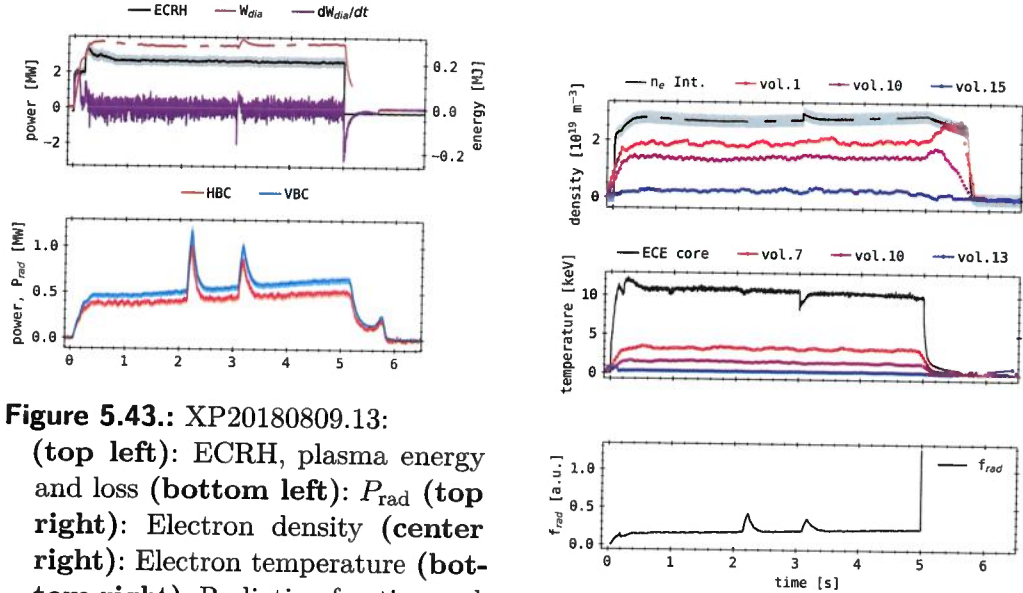


Figure 5.43.: XP20180809.13:

(top left): ECRH, plasma energy and loss (bottom left): P_{rad} (top right): Electron density (center right): Electron temperature (bottom right): Radiation fraction and target heat load.

Unit!

stored energy increases sharply in the beginning to 0.29 MJ and also steadily remains here besides a small positive bump at the time of the second blow-off. Its derivative therefore consists largely of null-level noise except in the beginning and during that minor peak, i.e. up to 2 MW and $-2\text{--}1$ MW respectively. The bolometers P_{rad} increases initially to 0.4–0.5 MW and overall steadily grows to 0.5–0.7 MW between the two cameras before decaying, with a secondary peak to 0.3 MW in 5.7 s, 0.7 s after the input heating is turned off. As mentioned before, the two LBO events are highlighted here by large maxima of 1.4 MW in $\underline{2.25}$ s and 1.2 MW in $\underline{3.25}$ s. Both camera results are qualitatively in good agreement and are only separated, growing with discharge time by <0.1 MW. The indicated confidence intervals of those do not exceed ± 50 kW. From inside to out, the electron density decreases from $2.5\text{--}0.3 \text{1/m}^3$ in the interferometer measured to the most outward TS volumes, however remaining relatively constant throughout the discharge. Only in 3 s a small peak in the line integrated n_e indicates a secondary injection of impurities. The same is true for the corresponding temperatures of 11 keV down to null, hence the discrepancy between ECE provided values and TS volumes is significantly increased. Inner- to outermost, the

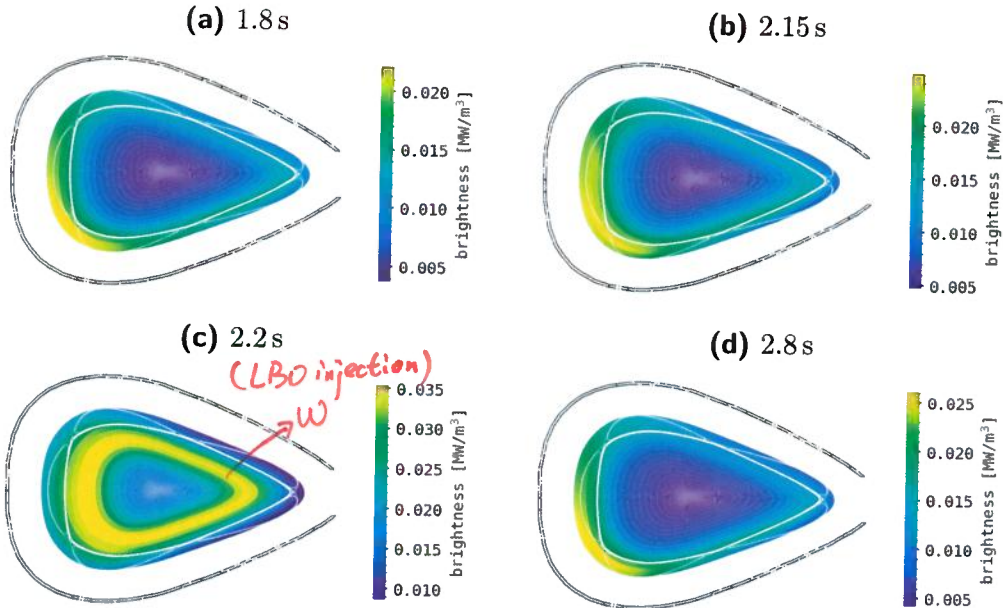


Figure 5.44.: XP20180809.13:

Tomographic reconstruction of experimental bolometer data on a $1.35 r_a$ inversion grid of standard magnetic configuration, otherwise similar to figure 5.42, between 1.8–2.8 s. RDA parameters are ~~constant~~ unchanged at $k_{\text{core}}, k_{\text{edge}} = \{2, 0.5\}$ and $N_T = 14, N_S = 2$. Corresponding ~~central~~ experiment parameters can be found in figure 5.43.

latter though only yield 3.5–1.8 keV, while volume no. 13 constantly read zero. During the first only negligibly and after the second ablation, $T_{e,\text{ECE}}$ instantaneously drops from 11–8 keV, before quickly and steadily growing back to the previous level. Finally, as stated above, the f_{rad} remains low throughout the experiment at <0.3 a. u., only breaching that threshold in correspondence to the laser blow-offs to a maximum 0.4 a. u.

The selected points in time for the performed reconstructions in figure 5.44 coincide with just before $t = 1.8$ s, during 2.15–2.2 s the first and again equilibrated after the second event in 2.8 s. Again, they are all produced using the same set of $k_{\text{ani}} = \{2, 0.5\}$ and parameters $N_T = 14, N_S = 2$. Here, the underlying magnetic configuration for the experiment and constructed two-dimensional mesh is standard., whereas the domain size has been inflated

reason ?

slightly more to $1.35r_a$. Plot (a) shows a maximum brightness outside the separatrix of particular, increased poloidal width, on the lower inboard side closest to the corresponding X-point of 22 kW/m^3 . Along the LCFS, the smooth intensity profile shows a relatively constant 15 kW/m^3 , though a very minor up-down asymmetry of $\pm 2 \text{ kW/m}^3$ is indicated.

In $t = 2.15 \text{ s}$, after the injection of secondary impurities but before a bolometer measured response in plasma radiation, minute changes in the absolute level of emission and its radial position hint at a contraction of the latter ring. The highest emissivity here is 25 kW/m^3 . One can also now notice a similarly bright inboard island of 23 kW/m^3 , expanding further on the lower peak from before. The rest of the profile is barely, if at all shifted inwards.

Around During the maximum in P_{rad} at $t = 2.2 \text{ s}$, the total emissivity is, on one hand significantly increased to 35 kW/m^3 and on the other essentially constant in a fixed radius $\sim 0.7r_a$ and FWHM of $0.15r_a$ on the inside of the separatrix. On the outboard side, the tomogram is distinctly limited, i.e. no radiation is reconstructed beyond the radial decay of the ring. Toward the inboard boundary, the (half-)width of the profile is increased to $0.25r_a$ and hence a considerable brightness still can be noted beyond the corresponding island structure. Conclusively, for $t = 2.8 \text{ s}$ in figure (b) at which the plasma radiation again has equilibrated but before the second LBO, a qualitatively congruent emissivity distribution is presented. While the absolute power level is increased slightly to 26 kW/m^3 and the radial decay towards the outboard tip of the triangular plane is shortened, the remaining tomogram is otherwise the same as in $t = 1.8 \text{ s}$.

This set of MFR shows two major characteristics of interest with respect to the introduced data in figure 5.43: first the contraction of the radiation distribution and its evolution under injection of external impurities and second the subsequent equilibration thereof. Introduction of additional high-Z material into the discharge leads to a reduction in T_e under constant or minor increase of plasma stored energy and large power dissipation through core radiation. The lack of precise temporal correlation between P_{rad} and the other plasma parameters during that event is not yet entirely understood. However, correlation tests, for example superimposing the outermost channels of the bolometers with the ECRH, have shown no significant deviation and therefore ruled out lagging of the prior in this context. No feedback was performed in this case, i.e. no parasitic computational load on the system like in section 3.2.1 is noted. The consequential centralisation of radiation is the

core

5.4. Tomography of Experimental Data

✓ result of the strong ionization of said material and hence its transport across the separatrix into the core. At this time, the plasmas' emissivity is entirely dominated by the quasi equilibrated impurity distribution producing the smooth and constant profile aligned in the center and along the LCFS. The asymmetry or shift of the maximum brightness towards the inboard side is attributed to a combination of magnetic configuration, the location of the bolometer inside the W7-X vessel, the low f_{rad} and therefore condensation of radiation in the LOS in and close to X-points. Lastly, this process proves to be reversible, as the ablated impurity is then again kinetically transported to the SOL and ejected from the plasma after relaxation of the central parameters. Again, this set of experimental MFR are well in agreement with the previous extensive verification benchmarks and accompanying diagnostic data in figure 5.43.

XP20181010.32

The next experimental data tomography concerns the prime real-time bolometer feedback application in XP20181010.32. Background plasma parameters and scenario configurations have been thoroughly and extensively illustrated in section 3.2.3 and more specifically figure 3.20. A selected set of points in time and tomograms have been produced in order to highlight the effects of the supplementary injection of gas ~~impurities~~ through the *thermal helium beam*. The results can be seen in figure 5.45. Regarding the previous reconstructions, similar or identical settings have been used to find the corresponding tomograms, though the experimental scenarios are vastly different. As one can already tell from taking a glimpse at the plot collection below, the characteristic features here are distinctly pronounced and in stark contrast to the latter images at the same time.

In (a) for $t = 0.65$ s during a small plateau, i.e. before the injection via the thermal gas valves has begun and at low $P_{\text{rad}} = 1.5$ MW and $f_{\text{rad}} \sim 0.25$ a. u., the first tomogram yields a largely radiationless or dim profile of a maximum 0.3 MW/m³, which is found very concentrated, close to the lower inboard X-point and inside the lower outboard island. Secondary features of a lesser intensity ~ 0.2 MW/m³ are located next to the upper central X-point, as well as in and around the lower inboard island. In-between these structures, sporadic emissivity of < 0.15 MW/m³ is scattered around the separatrix, mostly in the SOL but not outside $1.3r_a$.

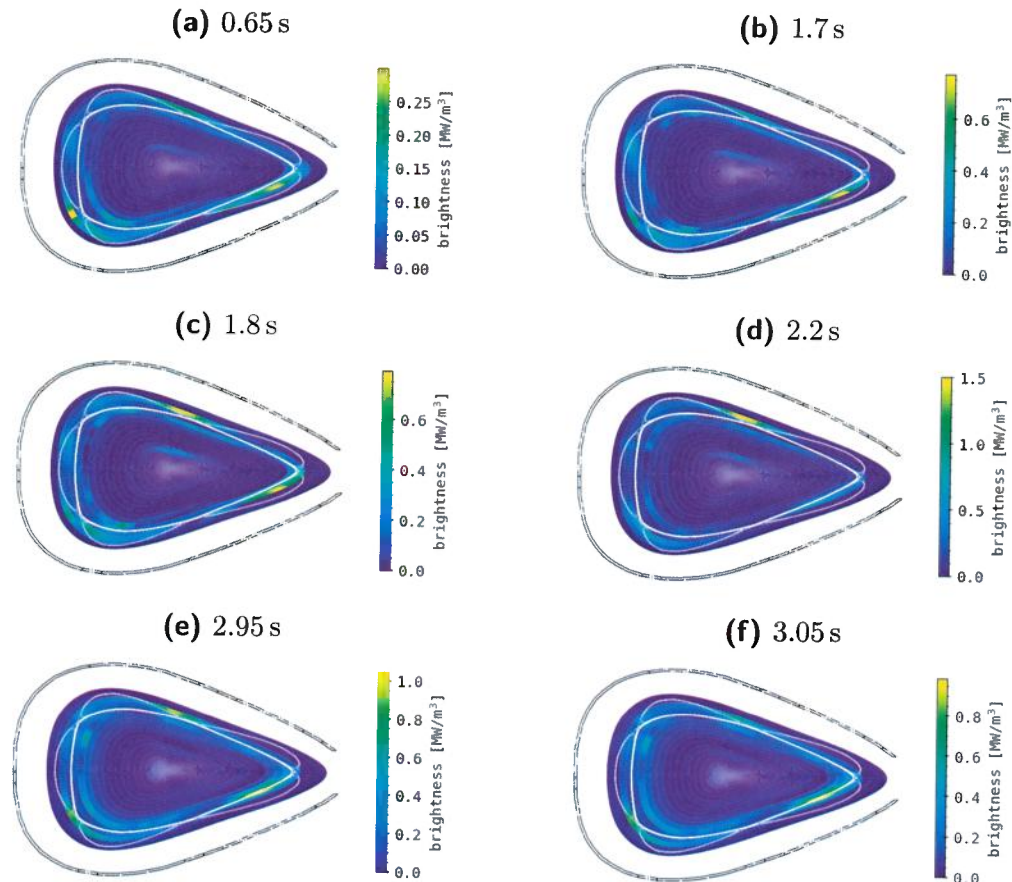


Figure 5.45.: XP20181010.32:

Tomographic reconstruction of experimental data on a $1.35 r_a$ inversion grid with $n_r \times n_\theta = 30 \times 150$, based off of standard magnetic configuration. Throughout 0.65–3.05 s, the RDA parameters are constant at $k_{\text{core}}, k_{\text{edge}} = \{2, 0.35\}$. Corresponding central experiment parameters have been previously introduced in figure 3.20.

In Fig. 5.43, ?
 $\{2.0, 0.5\}$ is used.

Then, at 1.7 s, the overall quality of the profile does not change, though the only remaining maximum is than in the lower island at the tip of the triangular shaped plane. Its brightness is also greatly increased to 0.77 MW/m^3 , while the relative intensity of the other previous extremes around the X-points is reduced. At that time, the QSB has continuously injected helium

5.4. Tomography of Experimental Data

(small amount; only for diagnostics)

as an impurity into the SOL and the ECRH has reached its steady-state power level. In terms of plasma profiles, density, temperature and radiation are strongly increasing at this moment still.

With the earliest equilibration of n_e and T_e , $t = 1.8$ s shows an emissivity distribution of similar magnitude - slightly increased to 0.78 MW/m^3 -, however now with the primary, global maximum in the upper central X-point and the previous decreased minutely. Outside those, the profile remains largely unchanged. Shortly after in 2.2 s for figure (d), a strong injection sequence of the thermal gas inlet feedback valves is concluded and P_{rad} has a first preliminary maximum of 4.5 MW. Simultaneously, electron temperature and density show minor peaks across the spatial spectrum. At this time, f_{rad} reaches 75% and the radiation power distribution condenses almost entirely to 1.5 MW/m^3 in a singular, confined point close to the intersection of the two upper magnetic islands. Relatively, no significant other structures stand out, though in locations of previous extremes emissivities of up to 0.6 MW/m^3 can be noted.

Next, at 2.95 s in figure (e), the radiation fraction has decreased again to a temporary minimum of $\sim 80\%$ in reaction to another full flow feedback injection pulse of 0.3 s and its shut-off. At the same time, T_e shows a minor minimum, while n_e yields a small maximum across the included diagnostics and TS volumes. The total integrated radiation power loss has now essentially reached its *quasi steady-state* level, given the oscillations due to the gas valves opening and closing, of 5–5.5 MW. The overall maximum brightness in the corresponding tomogram is lowered however to 1.05 MW/m^3 , though the number of highlighted features of that intensity is increased. Besides the previous localisation in the upper central X-point, the concentrated emissivity of the lower outboard island is now the global maximum and moved inwards onto the LCFS. A secondary structure at the lower inboard X-points yields 0.85 MW/m^3 .

Finally, tomogram (f) at $t = 3.05$ s corresponds to an f_{rad} of $\sim 95\%$, also coinciding with a preliminary maximum in T_e and minimum in n_e . This takes place while the QSB valves are closed and no additional gas injection is performed for another 0.1 s. In the conclusive two-dimensional radiation distribution, the brightest feature of 0.97 MW/m^3 is located again on the separatrix close to the lower outboard island, while previously noted localisations are reduced in intensity to $\leq 0.7 \text{ MW/m}^3$. With respect to the remaining, more or less sporadic profile, its relative emissivity is more akin

to that in 2.95 s and 1.8 s, i.e. less condensed to the aforementioned extremes. This sequence of MFR profiles provides a fundamental insight into the behaviour and impact of high- f_{rad} radiation feedback controlled thermal gas injections. It also graphically highlights the before outlined difficulty of defining and finding an ideal or even adequate LOS combination for the real-time bolometer evaluation metric - see section 3.2 and section 4.3. Both can be reduced to the very pronounced focussing of emission in points of intersecting closed field lines in the SOL and magnetic islands. Throughout the temporal evolution of the emissivity distribution, this characteristic is presented by a noticeable and significant correlation with the, however indirectly, feedback controlled radiation fraction. Up to 80% of f_{rad} , the majority brightness condenses and shifts from the lower outboard in counter-clockwise direction towards the upper central X-point. Beyond this level, though at a significantly increased absolute power, this trend is reversed and, with the radiation fraction growing towards unity, the majority of emissivities move to the lower outboard island. This process in itself is again reversible and between 80–100 %, this reallocation goes back and forth with the opening and closing of the thermal helium beam valves. That said, only during opening of said valves and injection of gaseous impurities, brightness profiles like in (d) are measured and the plasmas' response leads to conditions as in (e)-(f). This is on one hand due to the location of the gas inlet and its connection along magnetic field lines to the bolometer measurement plane, and on the other the combination of f_{rad} level and plasma profiles. The latter means that emissions are *pushed out* towards the separatrix and SOL, as the temperature and density distributions peak and centralise, meaning a sharp drop-off at that radius - see the extensive STRAHL simulations based on data from this discharge in section 4.4. Hence, the tomograms find the majority of emissivities only in these particular locations for $r \geq r_a$.

Regarding the configuration and selection of LOS for the real-time radiation estimate P_{pred} , this behaviour makes it particularly difficult to find an ideal or fitting set to adequately measure the power throughout the experiment. Hypothetically, a predictive collection only looking at the upper- and inboard-side SOL from both bolometer camera arrays inevitably overestimates, while in this case the opposite certainly underestimates the actual, total radiative power exhaust. A balanced set that watches all the above characteristics and also possibly integrates through intermittently lit areas is of great importance towards the success of such an application.

5.4. Tomography of Experimental Data

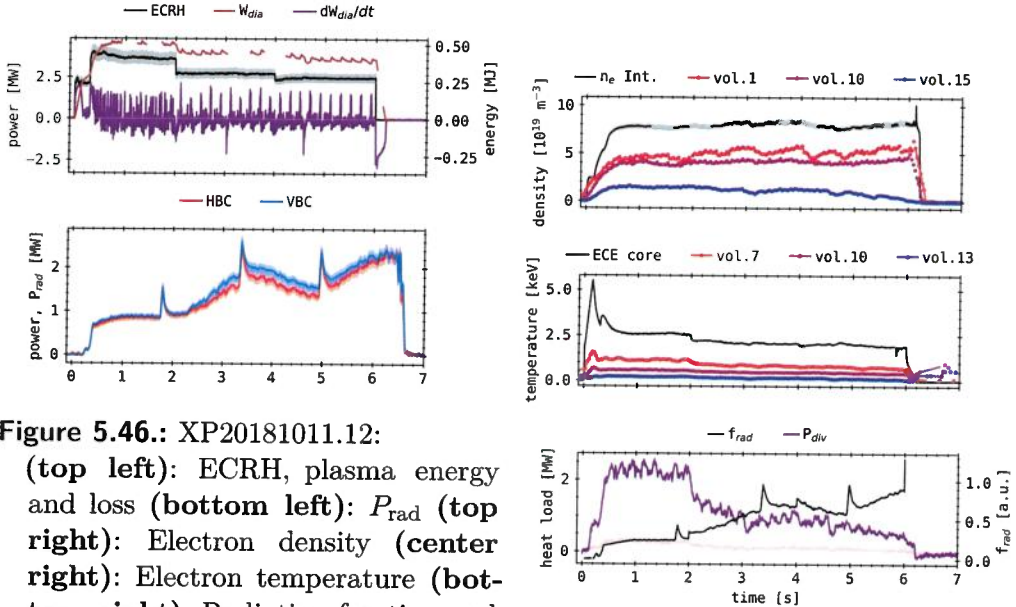


Figure 5.46.: XP20181011.12:
(top left): ECRH, plasma energy and loss
(bottom left): P_{rad}
(top right): Electron density
(center right): Electron temperature
(bottom right): Radiation fraction and target heat load.

In conclusion, the presented results and their interpretation are essential for following real-time, bolometer controlled radiation feedback experiments. However, the limited set of effectively one data point in XP20181010.32 makes predictions difficult.

XP20181011.12

The final example of experimental bolometer data *Minimum Fisher tomographic reconstruction* is given by XP20181011.12, of which the ~~core~~ plasma parameters are shown in figure 5.46 and the respective two-dimensional emissivity distributions in figure 5.47. This discharge is mostly characterised by two input power step-downs in the ECRH and intermittent impurity injections via the *laser blow-off* system, leading to, on one hand very pronounced events and on the other larger gradients in P_{rad} . *Which gradients?* The heating power in the top left of figure 5.46 begins with a small step of 2 MW until 0.3 s and follows with the first plateau at 3.5 MW for 1.7 s. After, P_{ECRH} is reduced to 2.7 MW for the next 2 s, until it finally drops to 2.5 MW for the remaining 2 s of discharge duration. Accordingly, W_{dia}

gradually increases to 0.27 MJ and then 0.5 MJ for the first major step in input heating. On top of that and throughout the rest of the experiment, minor oscillations of ± 50 kJ can be noted in the diamagnetic energy. With the first step-down in power, W_{dia} drops 0.1 MJ and at the conclusive second another 50 kJ before quickly decaying after ECRH shut-off. Its derivative largely reflects the described variations with temporally correlating ± 2 MW. Both bolometer camera results are qualitatively in good agreement, while the VBC estimates P_{rad} to be ≤ 0.3 MW larger in some places. The radiation power increases with a noticeable delay of 0.3 s to 0.8 MW, of which the equilibration is interrupted by the first LBO event in 1.7 s, leading to a peak of 1.7 MW. After the heating power step-down in 2 s, the radiative power loss near linearly grows to 1.8 MW in 3.3 s, at which the second ablation into the SOL takes place and causes a maximum of 2.7 MW. Afterwards, P_{rad} decreases again to 1.6 MW, simultaneously to the corresponding ECRH reduction, before the last impurity injection produces a peak emissivity of 2.6 MW in 4.9 s. The final 1.6 s of plasma radiation are dominated by an additional, steady growth to 2.5 MW before its collapse.

In the top right of figure 5.46, the plasma electron density remains generally constant throughout the discharge, after an initial increase, around $8\text{--}1.5 \text{1/m}^3$ from the inner- to outermost measurements. Neither LBO events nor ECRH steps appear to perturb n_e in these diagnostics and volumes significantly, though volume no. 15 decreases slowly over time until it almost measures null at the termination of the experiment. A similar picture is presented by the respective temperature, however T_e as provided by the ECE core diagnostic finds a large peak of 6 keV with a subsequent parabolic decay to 2.5 keV. This value also responds with minor decrements of 0.1–0.2 keV to the heating power step-downs, concluding the discharge at 1.9 keV. To a much smaller extent, the innermost *Thomson scattering* volume also presents this behaviour, peaking at 1.5 keV and equilibrating after 2 s around 1 keV. Measurement performed further outward remain relatively constant at even lower temperatures.

The radiation fraction generally follows the shape of the P_{rad} profile since the ECRH is constant with respect to its plateaus. In 2 s and 4 s however, a small jump in f_{rad} is visible due to the step-down in input power. At the end of the experiment, where P_{rad} is near maximum and P_{ECRH} at its lowest level, the radiation fraction reaches 0.85 a. u., while its global maximum is 0.93 a. u. at the second LBO ablation. Integrated and individual target heat

5.4. Tomography of Experimental Data

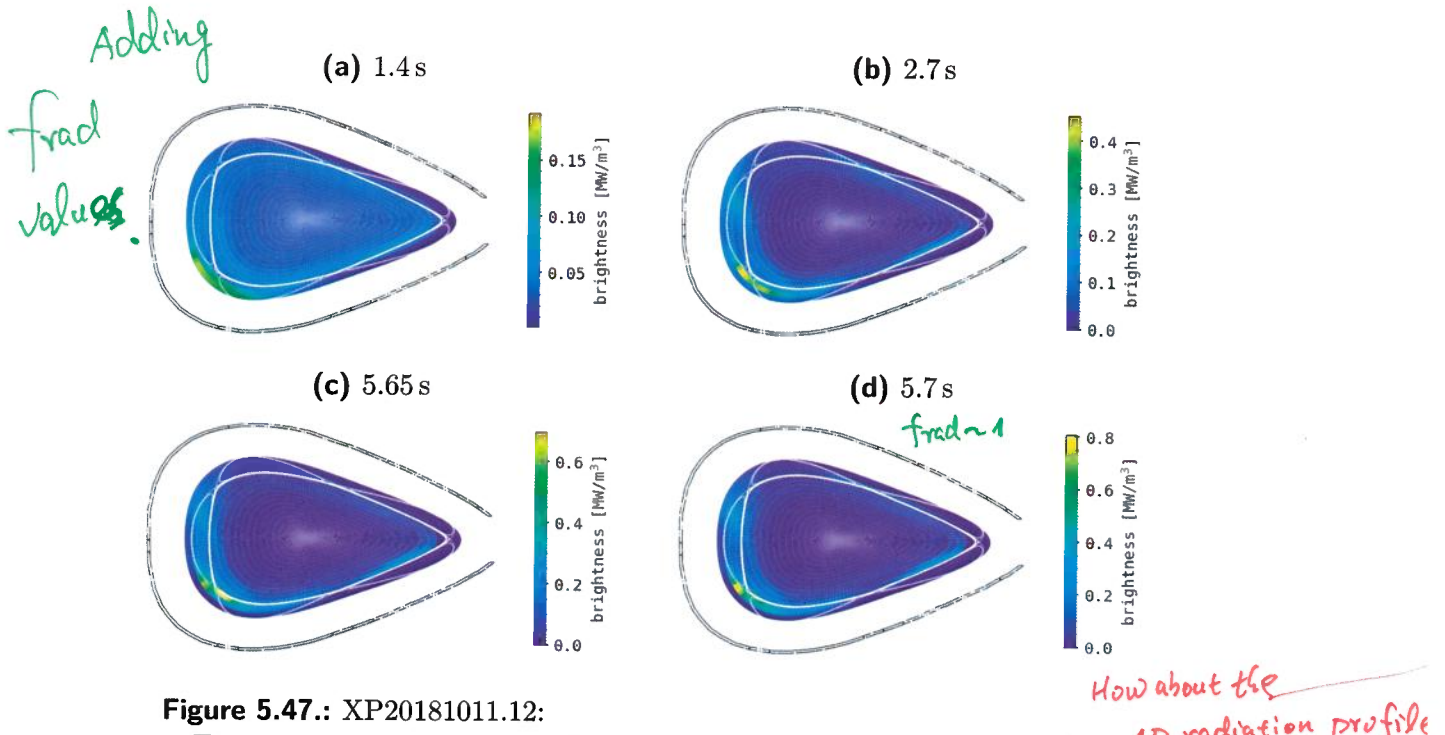


Figure 5.47.: XP20181011.12:

Tomographic reconstruction of experimental bolometer data on a $1.35 r_a$ inversion grid with $n_r \times n_\theta = 20 \times 150$ intersections, based off of the *KJM* high mirror magnetic configuration. RDA parameters are constant throughout at $k_{\text{core}}, k_{\text{edge}} = \{2, 0.35\}$ and $N_T = 14, N_S = 2$. Corresponding ~~central~~ experiment parameters can be found in figure 5.46.

loads show an inverse behaviour, the total P_{div} being largest around 2.3 MW during the first ECRH plateau and decreasing with the corresponding step-downs to first ~ 0.9 MW and then further gradually to 0.2 MW at the end of the discharge.

Figure 5.47 shows tomographic reconstructions of the respective bolometer measurement at four selected points in time. This experiment and hence the underlying MFR mesh are again based in a *high mirror field* magnetic configuration (*KJM*). Employed anisotropic regularisation weighting coefficients and parameters are kept constant at $k_{\text{ani}} = \{2, 0.35\}$ and $N_T = 14, N_S = 2$, similarly favouring smooth core and localised SOL emissivities. In (a) at $t = 1.4$ s, the radiation is near evenly distributed inside the separatrix at the outboard side, magnetic islands on the bottom, top and the

inboard side domain boundary with around 0.12 MW/m^3 . Only on the outside of the lower inboard X-point a strong and radially focused maximum of 0.19 MW/m^3 with a poloidal width of $\sim 0.125 \text{ rad}$ can be found. Minor variations $\leq \pm 0.01 \text{ MW/m}^3$ are presented along the lower inside the LCFS and in the core for $r < 0.7r_a$. At $t = 2.7 \text{ s}$ in figure (b), the inboard localisation slightly shifts radially towards the X-point and is now only one cell wide, while its emissivity increases to 0.45 MW/m^3 . Simultaneously, the overall brightness in the core and closer to the tip of the triangular plane remains constant, therefore decreasing significantly in relative terms. On the inside of the lower outboard island, towards the inboard structure as well as in its neighbouring islands, the intensity is raised to $0.25\text{--}0.3 \text{ MW/m}^3$. In (c) at $t = 5.65 \text{ s}$, the same behaviour as before is presented, now with a maximum emissivity of 0.7 MW/m^3 and secondary features at $0.3\text{--}0.4 \text{ MW/m}^3$. However, the localised characteristic has separated and expands now from the inboard magnetic island to the separatrix and X-point, where the peak lies. Finally, at 5.7 s in (d), the overall and maximum radiation density are increased again to $0.4\text{--}0.5 \text{ MW/m}^3$ and 0.8 MW/m^3 respectively. Now, the brightest feature is pushed outward again towards the edge of the inboard island and the inner structure is dimmed slightly.

~~The distribution of emissivity and its evolution throughout the course of this discharge is dominated by the characteristic condensation at the lower inboard X-point. Indications thereof can be seen in figure 5.42 at $t = 3.05 \text{ s}$, i.e. the tomogram with the highest f_{rad} in this sequence, however the configuration of the experiment and condition of the machine did allow for and achieve this particular profile of radiation. Experiment XP20181011.12 took place after the second boronisation of the W7-X vessel - a cleaning process and condition of the first wall using diborane gas and long duration glow discharges, after which the performance in terms of radiative power loss, impurity content, plasma density and temperature at a given input power is greatly improved. Hence, the qualitative structure of this set of tomograms is more akin to high radiation fraction experiments like XP20181010.32 etc., with the majority of emissions in the SOL and separatrix. However, in the first reconstruction at the lowest f_{rad} , the brightness beyond the LCFS is comparatively smooth, contrary to the corresponding $k_{\text{edge}} = 0.35 \text{ a.u.}$ which emphasizes anisotropic profiles. After a heating power step-down and external impurity injection, a similar contraction of emissivities like before applies to this distribution, condensing the now much larger total power to~~

a singular point. Further P_{ECRH} reduction, repeated ablation and therefore increase in radiation fraction conclusively leads to an inward shift of that feature. Finally, beyond that f_{rad} threshold and total intensity due to another decrease in input power and LBO event, this begins to move outward again, though in and along the respective magnetic island.

Regarding the performance of the MFR itself, the perhaps at this point generalizing k_{ani} weighting parameter configuration yields plausible results of adequate quality and is able to differentiate between minute changes between the selected profiles. The presented two-dimensional radiation distributions are also in line with the previously featured phantom image and experimental data reconstructions, i.e. transitions and proportions are in well in agreement with before. Particularly the capability to resolve single cell variations in location and brightness across a smaller range of intensity levels is proven here, especially given the increased uncertainty in actually measured data.

This concludes the, albeit limited application of the introduced and benchmarked MFR tomography algorithm on experimental bolometer data. Presented results have been achieved with confidence, particularly in light of the benchmarks performed in the previous section and underline the capabilities of said method. However, this is certainly only a, as was stated in the beginning, proof of concept. Implications should in no way be interpreted as generalized deductions, applicable to arbitrary input profiles, more so when taking into account the practically infinite experimental parameter space available.

5.4.1. Tomographic Reconstruction Statistics

The final step of this thesis is a *pseudo-statistical* analysis of the accumulated phantom image and experimental bolometer data Minimum Fisher reconstructions with respect to properties already introduced in the benchmarking process. The goal here is to, on one hand find possible underlying correlations in these numbers for artificial radiation distributions and on the other evaluate the fit of the previous tomograms with their corresponding ~~core~~ plasma parameters, i.e. power balance and P_{rad} .

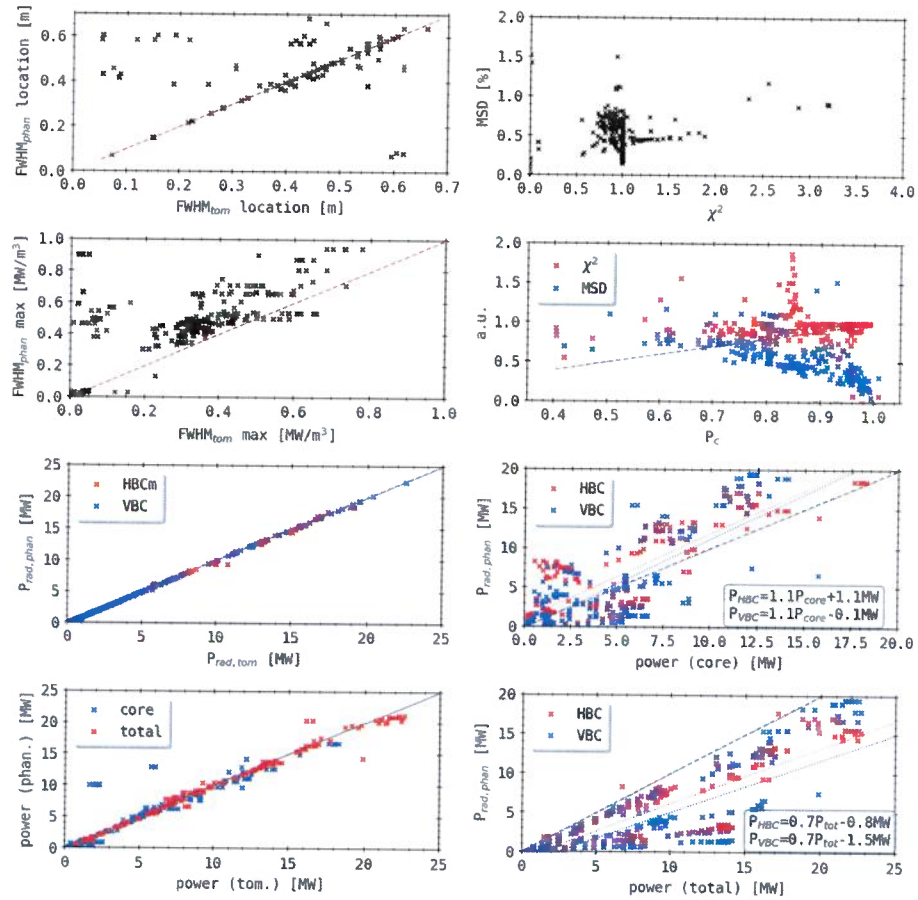


Figure 5.48.: Collected results of previously presented tomographic phantom radiation profile reconstructions in section 5.3. A red, dashed line indicates congruence between the two, i.e. 1:1 relation. **(left):** From top to bottom: FWHM position, FWHM maximum, P_{rad} from both cameras and two-dimensional, integrated emissivity. **(right):** From top to bottom: MSD over χ^2 , MSD and χ^2 over Pearson coefficient ρ_C , P_{rad} over integral of core emissivity and over total integrated radiation.

These are
from phantom
simulations.

Place this —
part in
5.3.5
or 5.3.6

Phantom Reconstructions

Not here.

First, combinations of the MFR phantom radiation image benchmark are collected and condensed into figure 5.48. Included are tomograms that yielded an absolute deviation from the phantom that is less than the integral of

5.4. Tomography of Experimental Data

the radiation distribution. In the left column of plots, the abscissa values are populated by data from the artificial input distributions, while the ordinate is defined by their respective tomogram match. The right column shows combinations of quality parameters MSD , Pearson coefficient ρ_c and fitness factor χ^2 , as well as the two-dimensional integrated powers and the individual P_{rad} extrapolations from the forward calculated detector signals. In all images, a 1:1 congruence line with 45° inclination is included to highlight ideal agreement in the data.

At the top on the left, the FWHM locations in the phantoms are compared to their reconstructed counterparts. However, as it was shown before, equality in number of radial extremes for both is not trivial, so value pairs ($FWHM_{\text{phan}}$, $FWHM_{\text{tom}}$) are produced here only where this is the case. Throughout the radial spectra, points are generally grouped close to or at the aforementioned line. Below, i.e. for tomogram maxima larger than their target, only a few outliers are measured, while for the opposite, $FWHM_{\text{phan}}(\text{loc.}) > FWHM_{\text{tom}}(\text{loc.})$ significantly more are found, particularly for greater discrepancies. Small groupings of points can be attributed to individual sets of one type of phantom image, e.g. a single bright ring or anisotropic island-like chains in the SOL. For the peak widths, the number of combinations is improved since every radial profile yields a result, as long as at least one extremum is produced. In the second plot, the corresponding maxima do not show a similar behaviour, presenting the input FWHM widths to be consistently larger. On average, $FWHM_{\text{phan}}(\text{max})$ is about 0.05 MW/m^3 larger than its reconstruction, whereas only a few points are below the line. Most results are grouped around $(0.35 \text{ MW/m}^3, 0.45 \text{ MW/m}^3)$, with smaller collections at the axis origin and $(0.075 \text{ MW/m}^3, 0.5 \text{ MW/m}^3)$. The next two plots compare P_{rad} from both forward calculated bolometer camera signals on the top and at the bottom the integrated two-dimensional radiation powers in the core and in total. The prior shows great congruence, with essentially only one outlier that yields an error $< 1 \text{ MW} \sim 10\%$. Otherwise, throughout the power spectrum $P_{\text{rad,phan}} = P_{\text{rad,tom}}$ within a confidence interval $\sigma_{\text{rad}} = 0.2 \text{ MW}$. No difference between HBCm and VBC is can be noted. Below, a similar picture is presented, with the majority of the results collected closely around the 1:1 slope. However, the spread is noticeably increased, with a $\sigma_{\text{rad}} = 0.7 \text{ MW}$ and a non-negligible amount of outliers, some in larger groups with $> \pm 1 \text{ MW}$ deviation. The integrated core and total emission, as well as tomogram and phantom values show no particular

difference across the power spectrum.

In the first plot of the right column of figure 5.48, the integrated average MSD is compared to the fitness factor between forward and backward calculated detector signals. A distinct line at $\chi^2 = 1$ between 0.1–0.8 % underlines the discrepancy among the quality parameters that was highlighted before during the benchmark. So does the group of results just below 0.5 %, spreading across $\chi^2 = 1.1$ –1.8 a. u. A larger cloud of points from 0.7 to just below the fitness factor reaching unity, stretching from 0.4–0.9 % similarly shows that the two-dimensional correlation not necessarily and positively correspond to the MFR targets. However, the few and sparsely spread outliers do show that the general significance of these quality parameters holds still, especially taking the lack of data for $\chi^2 > 1$ and >0.5 % into account.

In the next image, the previous two quantities are compared to the third estimate for congruence, the Pearson coefficient. Up to $\rho_c = 0.6$ a. u., almost no points are collected, with an initial smaller grouping of both parameters here around 0.8 a. u. Beyond, essentially separated by the indicated 1:1 line, χ^2 almost exclusively yields data above and the MSD below said feature. The prior shows points largely up to unity across the Pearson coefficients spectrum, with few outliers, a tight grouping of a large number of results closer to $\rho_c = 1$ a. u. and a particular column in 0.84 a. u. between $\chi^2 = 1.1$ –1.9 a. u. However, the MSD does the opposite, with the majority of its data below the line and a noticeable decay between 0.75–1 a. u. from 0.7 % to 0.2 %. Distinguishable clouds of points can be found along that near-linear trend.

The third plot of that column compares the individual cameras P_{rad} extrapolation from the forward calculated detector signals to the two-dimensional integrated power in the tomograms core. Additionally, separate linear fits for the HBC and VBC data are provided, including their parameters and colour-matched plot. Up to P_{core} and $P_{\text{rad}} = 7$ MW, data from both cameras is near equally distributed around the 1:1 line, with smaller, non-specific groupings, potentially corresponding to the same phantom image or MFR iterations thereof. For larger powers, only a small number of points can be found, particularly some outliers below the indicated line and the linear fit plots of both bolometer cameras. However, above said slopes, this amount is significantly increased and features distinct clusters around (7.5 MW, 12.5 MW) and (12 MW, 17 MW), including HBC and VBC data about equally. The corresponding linear fit function coefficients are calculated using a common

5.4. Tomography of Experimental Data

least squares regression algorithm, with P_{rad} and P_{core} as the in-/dependent variables respectively. The lines are represented by $P_{\text{HBC}} = 1.1P_{\text{core}} + 1.1 \text{ MW}$ and $P_{\text{VBC}} = 1.1P_{\text{core}} - 0.1 \text{ MW}$. Only the VBC plot intersects the 1:1 line for negligible powers, otherwise the fit functions exceed the core power consistently.

In the fourth and final image of the right column, the same plot is constructed with the total two-dimensional integrated power on the abscissa. Here, essentially all data points are under the 1:1 line, with the majority of those above both linear fits. Throughout the spectrum of tomogram emission levels, individual linear strings of results, their extrapolated trend originating in the coordinate origin can be found above and below, however not on the aforementioned regressions. The latter are given by $P_{\text{HBC}} = 0.7P_{\text{tot}} - 0.8 \text{ MW}$ and $P_{\text{VBC}} = 0.7P_{\text{tot}} - 1.5 \text{ MW}$. Most data is found in said line-like structures and smaller concentrations below $P_{\text{tot}} < 10 \text{ MW}$ and $P_{\text{rad}} < 10 \text{ MW}$. Above, those are spread out far more, however the general behaviour remains the same, with tighter groupings between the congruence and regression lines and noticeable point chains under the individual fits. At $P_{\text{tot}}, P_{\text{rad}} > 15 \text{ MW}$, particular horizontal feature of both camera results dominate the picture here.

Figure 5.48 visually highlights the deductions presented at the conclusion of the artificial radiation image benchmark of the introduced MFR algorithm. Results shown for FWHM location and value underline the radial matching capabilities, however at a lower fidelity in terms of the individual shape and given the discrepancy in multiplicity. The strong congruence in the comparison between bolometer camera radiative power loss extrapolations is evidence of, on one hand well preselected set of results and on the other equally effective tomography settings and success condition $\chi^2 = 1 \text{ a. u.}$ Similarly, the correspondence in absolute two-dimensional power values essentially adheres to the 1:1 line, however the degradation when compared to the above image is attributed to the intrinsic ill-posedness of the underlying inversion problem, i.e. large number of independent parameters. The same is true for the match between MSD and fitness factor, where for χ^2 approaching or at unity, the number of results increases and the tomograms' deviation is low, though still retains a noticeable spread and points are found far beyond that algorithmic cut-off. Overall characteristic and therefore conclusions here are reflected below in the comparison of fitness and Pearson coefficient, i.e. the concentrated results at $\chi^2 = 1 \text{ a. u.}$ towards

$\rho_c = 1$ and point clouds around there. The accompanying MSD data is in line with the interpretation of said two-dimensional quality measures, near linearly decreasing with increasing phantom-tomogram cross-correlation and vanishing at unity. Given this profile, the group of outliers in the previous plot and here above a fitness of 1 a. u. have to be certainly treated as such. They are connected to a particular set of artificial radiation distribution reconstructions of lesser adequacy - the corresponding MSD and ρ_c however indicate a good fit of tomogram and phantom. At last, the individual P_{rad} are not sufficiently represented by either the integrated core or total two-dimensional powers. The prior, at least for higher absolute radiation levels is potentially overestimated by the bolometer measurements, while their linear regression yields results supporting congruence at equal slopes for both cameras with minor absolute terms. Only the total radiation level presents somewhat linear coherence with P_{rad} of any camera, though at an arguably worse regression result, i.e. larger deviation of the corresponding plots from the 1:1 line and poorer parameters. Hence, the bolometers' extrapolation underestimates the - phantom contained - total emission, given the set of distributions and fits. The distinctive gap in results here suggests that for general groups of radiation profiles, more accurate predictive linear models could be calculated, though at possibly greater discrepancy to the ideal match of $P_{rad} : P_{2D}$ or even P_{tot} .

*The findings about kcore and kedge
are ...*

Experimental Data Reconstruction

Comparing MFR tomography results across different experiments statistically has proven difficult and so far has not produced substantial insight, however not beyond what was previously condensed from the established P_{rad} or chordal brightness data anyhow. This section will proceed and investigate the experimental inversions on a larger scale more closely, i.e. similarly to the evaluations above and for an applicable selection of parameters. The forward extrapolated and two-dimensional radiation powers in total and from the core are compared in figure 5.49. Collected data is selected only for $\chi^2 < 1000$, i.e. sensible results of the MFR and presented like before, including a line for exact identity of the quantities and plots for any respective linear regression fits.

The top image yields near ideal congruence of the forward and backward calculated P_{rad} from the experiment and tomogram. Except for lower total

5.4. Tomography of Experimental Data

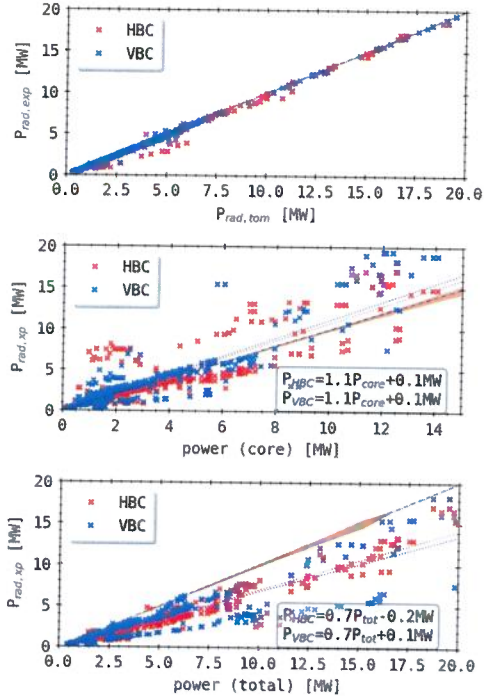


Figure 5.49.: Collected results of previously presented experimental data tomographic reconstructions in section 5.4. Included are reconstructions that yielded $\chi^2 < 1000$. A dashed 1:1 line indicates congruence between the axis and abscissa. If applicable, a regression linear fit for both cameras derived individually is noted in the bottom. A transparent error bar (orange) is indicated around the projected congruence. **(top):** P_{rad} of both bolometer cameras from experiment and tomogram. **(center):** P_{rad} of both cameras over integral of core emissivity. **(bottom):** P_{rad} of both cameras over total integral of emissivity.

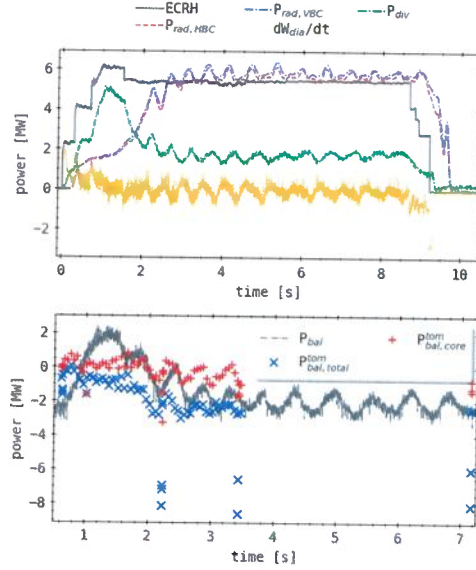
powers $< 7 \text{ MW}$, where the deviation of some HBC extrapolations is noticeably increased, the points follow the 1:1 line almost precisely. At most, a discrepancy of $\pm 0.75 \text{ MW}$ applies here across the spectrum. In the following image, the input detector measurement P_{rad} is compared to the core integrated two-dimensional power from the tomogram. Here, the dispersion of results is significantly larger than before, with a tighter grouping up to 7 MW. Particularly the VBC adheres to the direct proportionality for lower powers, however constantly by about 0.25 MW larger, while the HBC yields equally smaller values that tend to drop off quicker at those levels. For $P_{\text{core}} > 7.5 \text{ MW}$, this is replaced by a wider spread in both cameras around the 1:1 line, with slightly more points - especially the VBC - above said border, though still following the general trend. Across the spectrum, denser clouds of data with intervals of $< 0.2 \text{ MW}$ correspond to reconstructions for different settings of the same samples of the same discharge. A growing standard deviation with larger overall powers coincides with the aforementioned distribution of results. The respective regression fits are identical at $P_{\text{rad}}^{\text{HBC/VBC}} = 1.1P_{\text{core}} + 0.1 \text{ MW}$. Finally, the last image shows the same bo-

lometer measurements against the total integrated two-dimensional powers. Hence, overall similar behaviour is presented by the VBC and HBC up to 7 MW, though with a significantly lesser slope and therefore below the 1:1 line. Additionally, separate linearly increasing groups of points from the VBC in that range below the majority of data are shown. And again, beyond that threshold scattered values can be found around the fit lines, given by $P_{\text{HBC}} = 0.7P_{\text{tot}} - 0.2$ MW and $P_{\text{VBC}} = 0.7P_{\text{tot}} + 0.1$ MW. A standard deviation interval around the proportionality line also grows with the abscissa values until 16.5 MW, after which it vanishes.

Keeping in mind that the presented results are collected from various experiments - data is included also for reconstructions that have not been explicitly discussed or shown in this thesis -, particularly of very characteristic emissivity distribution and transitions, the correlation between these and the images shown figure 5.48 is quite significant. Especially given the very generous threshold interval in χ^2 for preselection, the congruence between the forward and backward calculated P_{rad} is on par with the deliberately designed and adjusted phantom profile tomography results. The strong agreement is hence certainly a testament to the performance and algorithmic optimisation of the MFR. Looking back at the comparison between the extrapolated and two-dimensional integrated power from the core, the linear regression fits and their underlying data are noticeably improved with respect to the target proportionality line for the experimental reconstructions. Not only do both camera measurements yield the same prediction function within a certain rounding error, which is simultaneously very similar to the direct congruence line, the points are generally grouped closer around follow the latter more closely. However, this means that P_{rad} underestimates the total, in the tomogram contained emissivity by an amount that is about equal to the radiation power in the SOL, since the last image shows in a comparable manner that P_{tot} is consistently larger. The latter is also reflected in the accompanying fit results, which still deviate only slightly between the cameras here. In conclusion, the small set experimental data MFR has shown very promising results both qualitatively as seen previously, but also quantitatively, especially in respect to the phantom benchmark. Though the strong performance of the algorithm in combination with actual measurements is diminished or in question due to the reduced set of assessable parameters, i.e. additional P_{2D} or ρ_c .

Figure 5.50.: XP20181010.32:

Comparison between previously derived power balance for XP20181010.32 in figure 3.22 and the balance calculated from the integrated two-dimensional radiation distribution of the tomographic reconstructions presented in section 5.4. **(top):** Central experiment parameters towards the power balance. **(bottom):** Comparison of power balances derived from a common P_{rad} and the radiation distribution integrals.



Power Balance

The final application and evaluation of MFR data is done using a selection of the previously presented experimental results for different points in time during the discharges and using these to calculate their respective power balance. Firstly, central plasma parameters for XP20181010.32 as introduced and discussed in figure 3.20, alongside said P_{bal} and individual points for each MFR tomograms total and core P_{2D} are given in figure 5.50. The prior is included as direct reference as before. Below, a power balance is constructed using, on the one hand the continuous P_{rad} from bolometer measurements as a profile and on the other the separate integrated two-dimensional core and total radiation powers from reconstructions of that experiment. For a detailed, in-depth treatment of the full P_{bal} see figure 3.22, though one should note here that particularly in the very beginning of the discharge and throughout the continuing feedback injections and corresponding oscillations, it consistently fails to achieve equalisation, even under consideration of the intrinsically large standard deviation. The individual results from the tomography are largely concentrated in the first 3.5 s of the experiment, except for a single MFR performed towards the end in 7.2 s. Calculating P_{bal} using the integrated emissivity only from the core of the reconstructed brightness distributions shows an overall much improved

match, i.e. $P_{\text{bal}} \rightarrow 0$. Until the first minor adjusting gas feedback around 2 s and except for a singular outlier, a maximum deviation of -0.5 – 1 MW can be noted, though on average it is below 0.5 MW. At the same time, the total tomogram contained radiation power, consistently larger in absolute terms, hence contributes to a reduced balance of -1.75 – 0.25 MW. Up to 2 s, both feature a hollow plateau-like profile, after which both drop noticeably with the first minor feedback cycle to -1.5 MW and -3 MW respectively. The core calculated balance relaxes after, however about 0.25 s more quickly than the reference plot, to around equalisation. Its total counterpart $P_{\text{bal}}^{\text{tot}}$ has the minimum and increase after the injection even before that with an additional 0.1 s earlier, though only up to -1.5 MW again. This behaviour is, except for the decreasing amplitude in oscillation for both and reduction in base level after relaxation for the total power balance, i.e. to -2 MW, repeated until 3.4 s. Here and at 2.2 s, the latter yields outliers in P_{bal} that are beyond -6 MW and therefore can be disregarded as results of faulty MFR configurations. At last, the reconstruction in 7.2 s and the tomograms' emissivity are in line with the previous observations, including the outlier at <-6 MW.

The presented power balance calculated using the integrated two-dimensional radiation distributions show a significantly different profile than for the corresponding P_{rad} extrapolation. A reconstructed core brightness is in much better agreement with the premise of $P_{\text{bal}} \rightarrow 0$ like discussed in equation (2.37), as deviations from equalisation and variations due to the feedback are reduced compared to using P_{rad} or $P_{\text{2D}}^{\text{tot}}$. The latter shows similar behaviour, though naturally at a greater distance from the target equilibrium, while still also featuring fewer oscillations by the injection of thermal gas impurities. In this particular case at larger radiation fractions, $P_{\text{bal,tot}}^{\text{tom}}$ increases its deviation from null and the core calculated value, though the latter remains close to $P_{\text{bal}} = 0$. With respect to the previously shown phantom tomography benchmark and experimental reconstruction statistics, this is generally in line with the established picture there and the corresponding linear regression fit results.

Both, $P_{\text{bal,tot}}^{\text{tom}}$ and $P_{\text{bal,core}}^{\text{tom}}$, are seen as a parameter for calculating P_{bal} , an improvement in qualitative and quantitative terms compared to the standalone extrapolation of detector measurements. Given the initial example, in special applications or for an optimised algorithm of allocating MFR samples - the computational load for a continuous solution thereby is hardly

5.4. Tomography of Experimental Data

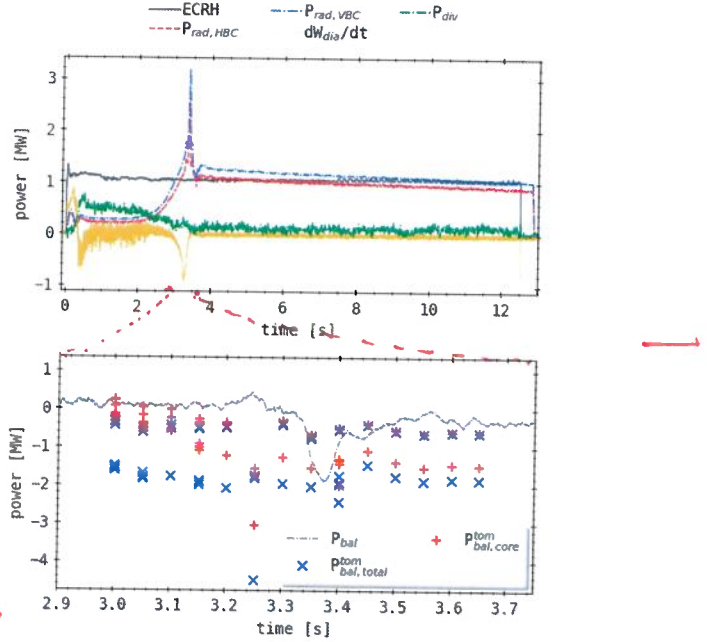


Figure 5.51.: XP20180725.44:

Comparison between power balances for XP20180725.44 as in figure 5.50. **(top):** Central experiment parameters towards the discharge power balance. **(bottom):** Comparison of power balances derived from a common P_{rad} and the radiation distribution integrals. (Symbol?).

2D

based on
line-integrals

practical -, this approach may prove to be a better radiation power loss measure towards a global power balance. While a second set of P_{bal} using reconstructed solutions will be featured, extending this to a statistical level for a more thorough and generalized evaluation is out of scope for this work.

The second example is presented in a similar manner as before in figure 5.51 for XP20180725.44. Central plasma parameters in the top image, as well as the plasma global power balance profile calculated using P_{rad} from the extrapolated detector measurements at the bottom have previously been introduced and discussed in figure 2.27, as well as figure 5.41 and the following MFR reconstructions. In conclusion, this has underlined the quasi steady-state applicability of the equation in equation (2.37) and difficulties during scenarios of fast or drastic plasma transitions. The current example features both rapid dis-/continuous changes in radiation regimes or events and steady-state equilibria. Results of reconstructed two-dimensional powers shown here are centred temporally around the mentioned plasma collapse and condensation of emissivity to the core towards 3.35 s between 3–3.65 s. Immediately noticeable is the consistent and almost constant separation not

only between the total and core integral calculated P_{bal} but also among those, indicating a significant quantitative difference for various MFR configurations, i.e. k_{ani} parameters. The power balance derived from P_{2D}^{core} is close to or slightly below equality and its P_{rad} counterpart up to 3.1 s and therefore the radiative loss too large. Individual points are still within 0.3 MW of each other, while $P_{\text{bal,tot}}^{\text{tom}}$ is close and inside that interval, though one set of results is ≤ -1.4 MW here. All decrease further and hence increase their distance from the reference profile with time until the event in 3.35 s. The discrepancy among the individual sets of points also slightly grows, as in 3.25 s the core and total reconstructed balance suddenly drop to -1.5 – -4.6 MW with gaps of 1.4–2.6 MW in a singular group of outliers. However, towards and across the plasma collapse, the two values and their separate levels remain relatively constant, with minor variations of ± 0.5 MW compared to the -1.8 MW reference drop. Throughout the series of reconstructions, the integrated two-dimensional powers lead to a continuously but slowly decreasing balance with a trend from 0– -1.5 MW to -0.5 – -1.8 MW. This variation is about double that of the P_{bal} profile reduction after the event. Beginning in 3.3 s and continuing, one $P_{\text{bal,tot}}^{\text{tom}}$ coincides with the higher $P_{\text{bal,core}}^{\text{tom}}$ and the differentiation within has equilibrated at that level. For $t \geq 3.5$ s, the tomograms yield nearly constant results in both parameters for all configurations.

Similar results as before in figure 5.50 are presented here, as the contribution of the core integrated tomogram emissivity fits better to the target equalisation of $P_{\text{bal}} = 0$ and the P_{rad} calculated reference than its $P_{2D,\text{tot}}$ counterpart. Furthermore, both are less impacted by the previously discussed stronger and faster transitions noted in the standard derived plasma power balance. Despite the steady-state development, the values computed using tomography results deviate significantly from their target and more so than for the feedback controlled discharge. Though the discrepancy between the two set of points and for varying MFR parameter configurations is also of similar magnitude. The worse match of $P_{\text{bal,core}}^{\text{tom}}$ hence is likely due to the characteristic shape of the underlying reconstructed brightness profiles in figure 5.42 particularly after the collapse, since essentially no emissivity is placed here for $r > r_a$. Again, the ratio between the tomogram powers is well in line with the prior statistical analysis. Overall, this still remains a valid estimator of the radiative plasma power loss and input to its total

equilibrium power balance.

5.5. Conclusions

This concludes the final physical chapter of this thesis and therefore the introduction, benchmarking and experimental evaluation of a tailored *Minimum Fisher regularisation* tomography algorithm for the multicamera bolometer diagnostic at W7-X.

Tests applying geometric perturbations and using different methods of sensitivity discretisation have shown significant robustness of the MFR against such variations and simultaneously established a set of configurations that provide adequate transmissivity at favourable computational costs. The impact of essentially unknown discrepancies of the actual *in-situ* orientation compared to an *as-designed* assembly of the bolometer have been estimated using forward calculation and found to be non-negligible. However, it was measured to be of similar magnitude as other variabilities to the MFR and hence indistinguishable in the final tomogram. At the same time, supplementary artificial camera arrays of deliberately tailored geometry, specifically filling gaps in the previously examined setup, were introduced to the tomography and used to aid in the reconstruction of more complex phantom radiation distributions. STRAHL simulated radiation profiles have revealed a noticeable asymmetry in the symmetrical designed bolometer LOS configuration and corresponding transmissivity matrix T , with a bias towards the upper separatrix area and SOL.

The benchmark has shown both the effectiveness and limits of said algorithm, underlining the existence of an ideal set of tomography parameters for a given input two-dimensional emissivity distribution. Anisotropy regularisation weight coefficients produced results of more localised ($k < 1$) or smooth ($k > 1$) radiation profiles as intended, hence corresponding also to improved quality measures ρ_0 etc. The latter have shown to not be exclusively congruent and suggest that the quantitative or qualitative optimal tomogram is not necessarily achieved for $\chi^2 = 1$. Experimentally motivated artificial phantom images were proven to be particularly difficult to reconstruct, therefore provided valuable experience towards the reconstruction of actual experimental data. Iteration in k_{ani} across a much larger set of profiles than presented has further cemented the above evaluations. Statistical

The results show

analysis across all artificial emissivity distributions similarly agreed with those assessments, while also producing linear regression results correlating the two-dimensional radiation power and forward calculated P_{rad} . Thereby, both cameras find that core emissions exclusively are slightly overrepresented, and the absolute integrated power significantly overestimated by their corresponding extrapolations.

Practical application of the established knowledge about the RDA-MFR algorithm, i.e. tomography of W7-X campaign bolometer measurements provided adequate and robust results, though does not yield insights beyond this initial impression due to its limited execution. However, evaluation of all experimental reconstructions combined presented nearly identical numbers compared to its artificial counterpart, evidently supporting the findings in this reduced set tomograms. Furthermore, at last, integrated powers were used to calculate global, *quasi steady-state* power balances for selected samples in time in comparison to the continuous P_{rad} profile. While no absolute improvement is measured for neither core nor total integral and the aforementioned discrepancy between P_{rad} and P_{2D} is observed here significantly, both are characteristically more stable and a potential alternative for small interval inspections.

The Minimum Fisher regularisation tomography algorithm in combination with the radially dependent anisotropy weighting has hereby been formally and thoroughly benchmarked and tested for the particular application with the multicamera bolometer diagnostic at W7-X. Conclusions are robust and promise overall reliable results, though one has to keep in mind the difficulty of multidimensional parameter optimisation during such ill-posed reconstruction problems. Combination with previous synthetic data and geometric perturbations was successful in outlining the shortcomings of this setup and providing hypothetical upgrades thereto.

the two-camera

$P_{\text{rad}, 2D}$
chord -
brightness
based

qualitative